Snow Depth Patterns in a High Mountain Andean Catchment from Satellite Optical Tristereoscopic Remote Sensing

Thomas E. Shaw, Simon Gascoin, Pablo A. Mendoza, Francesca Pellicciotti, James Mcphee

AGU100 ADVANCING EARTH AND SPACE SCIENCE

Water Resources Research

RESEARCH ARTICLE
10.1029/2019WR024880

Special Section:
Advances in remote sensing, measurement, and simulation of seasonal snow

Snow Depth Patterns in a High Mountain Andean Catchment from Satellite Optical Tristereoscopic Remote Sensing

Thomas E. Shaw[1], Simon Gascoin[2], Pablo A. Mendoza[1,3], Francesca Pellicciotti[4,5], and James McPhee[1,3]

[1]Advanced Mining Technology Center, Universidad de Chile, Santiago, Chile, [2]Centre d'Etudes Spatiales de la Biosphère (CESBIO), Toulouse, France, [3]Department of Civil Engineering, Universidad de Chile, Santiago, Chile, [4]Federal Institute for Forest, Snow and Landscape Research (WSL), Birmensdorf, Switzerland, [5]Department of Geography, Northumbria University, Newcastle, UK

Key Points:
- Pléiades snow depths are negatively biased and have inaccuracies for shallow snowpacks (<0.2m) and on steep slopes (>−40-50°)
- Ground-based and satellite information was used to fill gaps and generate an 'end-product'
- Model alternatives estimate -28% to +54% snow volume differences compared to Pléiades, even when locally calibrated

Supporting Information:
- Supporting Information S1

Correspondence to:
T. E. Shaw,
thomas.shaw@amtc.uchile.cl

Citation:
Shaw, T. E., Gascoin, S., Mendoza, P. A., Pellicciotti, F., & McPhee, J. (2020). Snow depth patterns in a high mountain andean catchment from satellite optical tristereoscopic remote sensing. *Water Resources Research*, *56*, e2019WR024880. https://doi.org/10.1029/2019WR024880

Received 30 JAN 2019
Accepted 18 DEC 2019
Accepted article online 21 DEC 2019

Abstract Obtaining detailed information about high mountain snowpacks is often limited by insufficient ground-based observations and uncertainty in the (re)distribution of solid precipitation. We utilize high-resolution optical images from Pléiades satellites to generate a snow depth map, at a spatial resolution of 4 m, for a high mountain catchment of central Chile. Results are negatively biased (median difference of −0.22 m) when compared against observations from a terrestrial Light Detection And Ranging scan, though replicate general snow depth variability well. Additionally, the Pléiades dataset is subject to data gaps (17% of total pixels), negative values for shallow snow (12%), and noise on slopes >40–50° (2%). We correct and filter the Pléiades snow depths using surface classification techniques of snow-free areas and a random forest model for data gap filling. Snow depths (with an estimated error of ~0.36 m) average 1.66 m and relate well to topographical parameters such as elevation and northness in a similar way to previous studies. However, estimations of snow depth based upon topography (TOPO) or physically based modeling (DBSM) cannot resolve localized processes (i.e., avalanching or wind scouring) that are detected by Pléiades, even when forced with locally calibrated data. Comparing these alternative model approaches to corrected Pléiades snow depths reveals total snow volume differences between −28% (DBSM) and +54% (TOPO) for the catchment and large differences across most elevation bands. Pléiades represents an important contribution to understanding snow accumulation at sparsely monitored catchments, though ideally requires a careful systematic validation procedure to identify catchment-scale biases and errors in the snow depth derivation.

1. Introduction

Seasonal snow cover is a crucial component of the global freshwater supply upon which millions of people rely for drinking water, hydropower, agriculture, and mining (Brown and Saldivia, 2000; Stehr & Aguayo, 2017). Within the semi-arid Andes of central Chile (33–36°S), the mountain snowpack is of significant socio-economic importance and is often in contrast to the limited, seasonally dependent precipitation measured at low elevations (Falvey & Garreaud, 2007; Meza et al., 2012). The strong elevation gradient between the coastal and mountainous regions of central Chile, combined with the lack of high elevation in situ data, inhibits the ability to prescribe suitable precipitation gradients and thresholds to estimate the quantity and distribution of snow (Mernild et al., 2017). Furthermore, patterns of winter snow at high elevations are dictated in large part by the interaction of topographical and meteorological factors, which complicate the estimation of the amount and timing of snowmelt (Freudiger et al., 2017).

The spatial heterogeneity of the snow cover can be attributed to local precipitation events that are strongly affected by the interaction of the terrain elevation with the local climate (Mott et al., 2013). The preferential distribution of initial snow cover on favorable slopes and aspects may be subsequently redistributed by wind (Essery et al., 1999; Gascoin et al., 2013; Lehning et al., 2008; Schirmer & Lehning, 2011; Trujillo et al., 2007) or avalanching (Bernhardt & Schulz, 2010; Ragettli et al., 2015), thus adjusting the shape of the seasonal hydrograph (Freudiger et al., 2017), the potential melt-sublimation ratio (Ayala et al., 2017), and the mass balance of glacierized basins (Gascoin et al., 2011; McGrath et al., 2015). Furthermore, the resulting spatial snow distribution can be governed by the radiation forcing of the surface slope relative to the local solar

zenith and azimuth angle of the sun (Ayala et al., 2014), promoting higher quantities of snow on north-facing slopes (in the Northern Hemisphere), and delaying melt onset. Several of the aforementioned studies have explored the relationship of topographical parameters from digital elevation models (DEMs) and seasonal snow depth, finding similar dominant controls, namely, orientation, slope angle, exposure to wind, and elevation, at a variety of spatial and temporal scales (Grünewald et al., 2013; McGrath et al., 2015; Zheng et al., 2016).

Localized processes such as avalanching and wind redistribution of snow over scales of tens to hundreds of meters, however, limit the generalizability of statistical models that estimate spatial snow depth based upon common relationship that it has with topographic features of a landscape (such as described above). For example, Grünewald et al. (2013) found that linear regression models built around topographic information of an individual study basin were able to explain as much as 91% of snow depth variations at that site, given a spatial resolution of 100 m. However, "global" model sets developed using all or multiple study sites were able to only explain up to 28% of the measured snow depths. Due to the lack of statistical model transferability (Grünewald et al., 2013), uncertainty of regional vertical precipitation gradients (e.g., Ragettli et al., 2014; Scaff et al., 2018) and the high computational demands for boundary layer wind flow models (e.g., Musselman et al., 2015) to obtain spatial snow depths, a data-rich measurement approach seems appropriate to characterize snow depth variability in high mountain catchments.

Point-based snow surveys are time consuming and potentially hazardous, restricting the sampling of an entire basin (Erxleben et al., 2002; López-Moreno & Nogués-Bravo, 2006). Automatic measurements based upon sonic depth gauges can provide a continuous record of snow depth, but similarly cannot account for snow spatial variability within a basin (Egli et al., 2009; Molotch & Bales, 2005). Developments of low-cost optical photogrammetry using unmanned aerial vehicles (UAVs) have demonstrated success at providing accurate snow depth maps (Jagt et al., 2015), though are limited to small spatial scales by controller range and battery capacity and may require high accuracy measured ground control points to be well distributed in the study location. Application of airborne Light Detection And Ranging (LiDAR) has also been fundamental to understand the spatial variability of snow depth at various locations around the world (Deems et al., 2013; Grünewald et al., 2013; Painter et al., 2016), though operational costs are high and surveys are still limited in their spatial coverage. Terrestrial LiDAR applications can potentially limit costs of their airborne counterpart and have been deployed to measure snow depth variability for individual (Prokop, 2008, Grünewald et al., 2010) and repeat surveys (López-Moreno et al., 2017). Nevertheless, gaps in the dataset can be caused by complex topography, convex landforms, large scanning distances, and beam divergence relative to the angle and orientation of the terrain features (Revuelto et al., 2014; Buhler et al., 2016; López-Moreno et al., 2017). Furthermore, spatial extent of terrestrial surveys are typically smaller than airborne LiDAR equivalents (Painter et al., 2016). Satellite products may resolve many of these issues and have been implemented for decades to observe changes in snow-covered area (e.g., Brown and Mote, 2009; Mernild et al., 2016). Nevertheless, these products are (1) of coarse resolution (ranging from 30 m [LandSat] and 300 m [Sentinel 3] to 25 km [AMSR-E]), (2) limited to clear-sky conditions (optical-based sensors), and (3) typically can only derive snow-covered area and provide reconstructed snow water equivalent at the end of the snow season only through indirect methods (e.g., Cornwell et al., 2016).

Marti et al. (2016) utilized tri-stereo photogrammetry from optical Pléiades satellites to derive snow depth maps at a spatial resolution of 1–4 m by differencing subsequent DEMs. This is a method that has been widely used to reconstruct changes in glacier volumes and winter mass balance (Belart et al., 2017; Berthier et al., 2007, 2014), but rarely used for snow volumes alone. Comparison with manual probe measurements and a UAV snow survey revealed a high consistency of spatial snow depth derivation (snow pack depths 0–15 m) and a promising approach for mapping snow in the open terrain of a Pyrenean catchment. This is a new approach, afforded by the high quality/accuracy of these satellite images. Nevertheless, the applicability of this approach to other, high mountain regions has been little tested to date.

Accordingly, we aim to derive the best possible dataset of snow depth using Pléiades satellites for a remote region where snow represents a critical water resource. Specifically, we aim to (i) derive a high-resolution snow depth map for a glacierized catchment in the Andes of central Chile, following the approach of Marti et al. (2016), evaluating it against a terrestrial LiDAR scan for a subregion of the study domain; (ii) generate a corrected and filtered Pléiades snow depth map; and (iii) compare the spatial snow depths to the

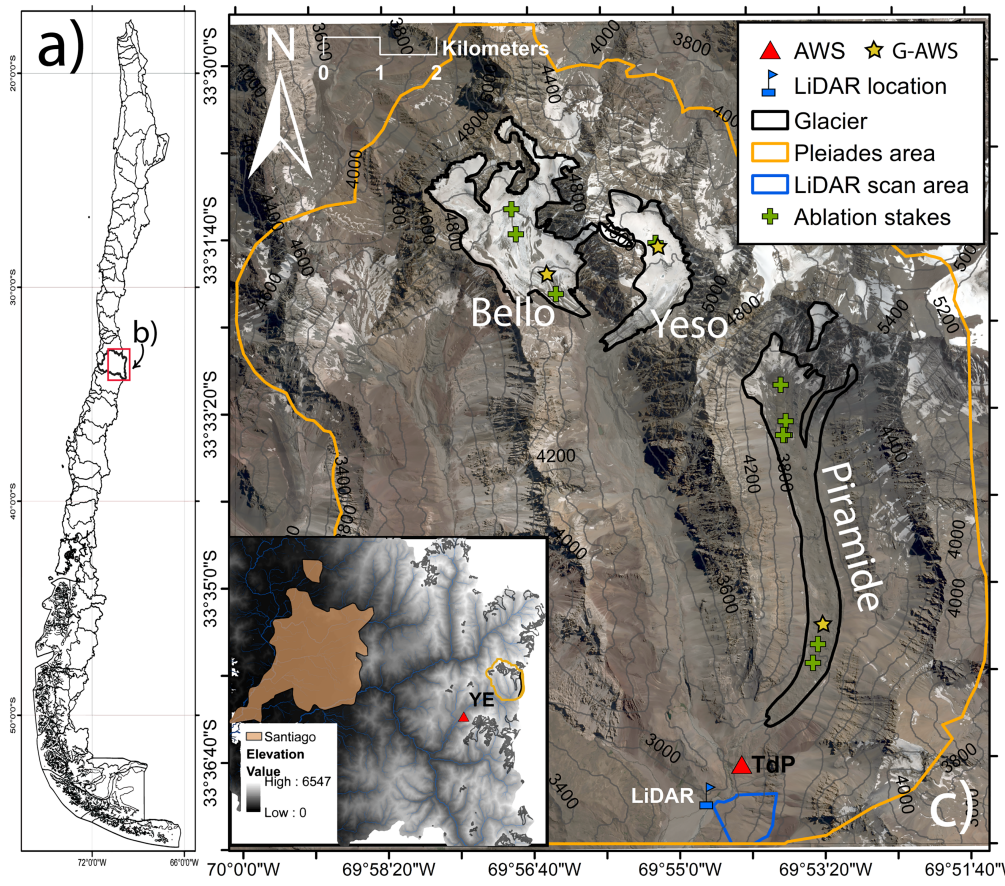

Figure 1. Map of the study basin, Rio del Yeso, with location of site within Chile (a) and the metropolitan region (b). The regional map in (b) shows the relative elevations of Santiago (brown region) and the Andes using an ASTER DEM (2011). Positions of the LiDAR (blue) scan as well as weather stations YE (in regional inset—b) and TdP (in catchment image—c) are shown. Ablation stakes and on-glacier AWS (G-AWS) relevant for glacier corrections (supplementary information) are given by the green crosses and yellow stars, respectively. Background satellite image source: PlanetScope (25/01/2018).

statistical method of Grünewald et al. (2013) and the physically oriented "distributed blowing snow model" of Essery et al. (1999).

2. Study Site

The Rio del Yeso catchment is located in the semi-arid Andes of central Chile (33.4°S, 69.9°W) and is at the headwaters of the Maipo River basin, which serves the country's capital, Santiago (Figure 1). The catchment covers an area of 102 km^2 (12% glacierized), with small sclerophyllous vegetation and an elevation range of ~2900–5400 m a.s.l. The basin is oriented predominantly to the south, with three steep sided valley corridors (mean slope of the basin is 27°) that join to an outwash fan. The three main glaciers of the basin are Bello (4.6 km^2), Yeso (2.9 km^2), and Piramide (4.7 km^2, debris-covered), which contribute between 3% and 32% of the basin's spring-summer streamflow (*Burger et al., 2018b*). The wider region exhibits a steep elevation difference between the Chilean coast and the eastern border with Argentina, resulting in a strong longitudinal climatic gradient additional to the pronounced climate seasonality, whereby the majority of the annual precipitation falls between May and September (Garreaud, 2009). Mean May-September air temperatures (1980–2017) at Yeso Embalse (10 km southwest of the study basin, 2475 m a.s.l.) are 3.5 °C, and the mean precipitation totals are 505 mm (86% of the mean annual sum) (http://explorador.cr2.cl/, last access: June 2018).

3. Data and Methods

3.1. LiDAR

A subregion of the study basin (Figure 1) was measured using a long-range terrestrial LiDAR scanner (Reigl VZ®-6000) that operates at a near-infrared wavelength (1064 nm), with a range exceeding 6,000 m for a good diffusively reflective target and an angular step resolution of up to 0.002°, making it highly suitable for monitoring changes of snow and ice in mountain environments (Fischer et al., 2016; Telling et al., 2017). We obtained a 0.74 km^2 scan for the dates 13 September (with snow, hereafter LID_Snow_{ON}) and 12 December 2017 (without snow, hereafter LID_Snow_{OFF}) for comparison of Pléiades vertical differences ("apparent snow depth"—section 3.6.2). The location of the LiDAR scanner position for both dates was measured using a differential-GPS Real Time Kinematic point (horizontal and vertical precision of 0.005 and 0.015 m, respectively). The raw point clouds (mean point density = 33 p m^2) were registered using manual cloud to cloud feature matching in the Reigl RiScan Pro software to identify common features of LID_Snow_{ON} and LID_Snow_{OFF} scans at each location. Points were then subsequently matched using an iterative closest point alignment based upon manually selected subdomains of both scans where snow was absent (e.g., exposed bedrock). The calculated error of the LiDAR point cloud matching was 0.025 m. The resultant vertical differencing of the rasterized point clouds (DEMs) provides the distributed snow depth map, exported with a resolution of 0.5 m and resampled to 4 m using cubic resampling for comparison with Pléiades. An error estimate for the LiDAR snow depths was derived by calculating the mean vertical difference of the LID_Snow_{ON} and LID_Snow_{OFF} DEMs for manually identified areas of the scan that contain permanent human structures or snow free areas, which should therefore be static. A propagation of the dGPS, point cloud, and DEM differencing error was calculated as 0.08 m.

3.2. Manual Snow Depth Measurements

Two sets of manual probe measurements of snow depth were obtained in September (lower catchment) and October-December 2017 (Bello Glacier). The LiDAR scan was accompanied by 56 manual probe measurements of snow depth, collected immediately after the scan on 13 September 2017. The location of each probe measurement (averaged between a forward, center, and two side measurements) was provided by a non-base corrected Trimble R4 rover unit (accuracy ~2 m). Although at relatively short scanning distances (<500 m), the comparison of the LiDAR rasterized LiDAR point clouds with the manual probe snow depths must be cautiously considered due to uncertainty in the exact position of the probe measurements. We utilize these probe measurements to validate the LIDAR scan as our "reference" snow depth map (see section 3.6.2) and compare the two methods using the original 0.5 m raster resolution of the LiDAR. We estimate uncertainty of manual measurements from possible human error and soil penetration by the probe to be 0.05 m. Bello Glacier snow depths represent an opportunistic sample of >150 measurements obtained during field campaigns along the longitudinal transect of the glacier, though using a handheld Garmin GPS (accuracy ~5 m).

3.3. Pléiades Images

We utilize tri-stereo optical imagery from the French Pléiades satellites (CNES) to derive 4-m DEMs, following the methodology of Marti et al. (2016). This posting was chosen to balance the lowest fraction of no-data area at the catchment scale with a comparatively small loss of accuracy. The three panchromatic images (480–830 nm) (Table S1) were used to generate DEMs using the multiview stereo approach in the NASA Ames Stereo Pipeline (Shean et al., 2016) for the end-of-winter snow conditions, close to assumed peak snow water equivalent (PLE_Snow_{ON}), and a majority snow-free condition (PLE_Snow_{OFF}). This was done using the *stereo* tool based on the rational polynomial coefficient files provided by operator and the alignment method was set to affine epipolar. We note that we do not intend a methodological development of the approach in this paper and therefore apply the same configuration as described Marti et al. (2016). As with Marti et al. (2016), the stereo-orientation from the rational polynomial coefficient data was enough to adjust the relative orientation of the images prior to their projections in the epipolar geometry. Both point clouds were converted to raster DEMs in the WGS-84 UTM 19S coordinate system using *point2dem* with a search-radius-factor of 1. Application of bundle adjustment for camera self-consistency improved intersection errors (Figure S1 of the supporting information), though resulted in large DEM tilt that was unconstrained due to lack of ground control points, and thus avoided.

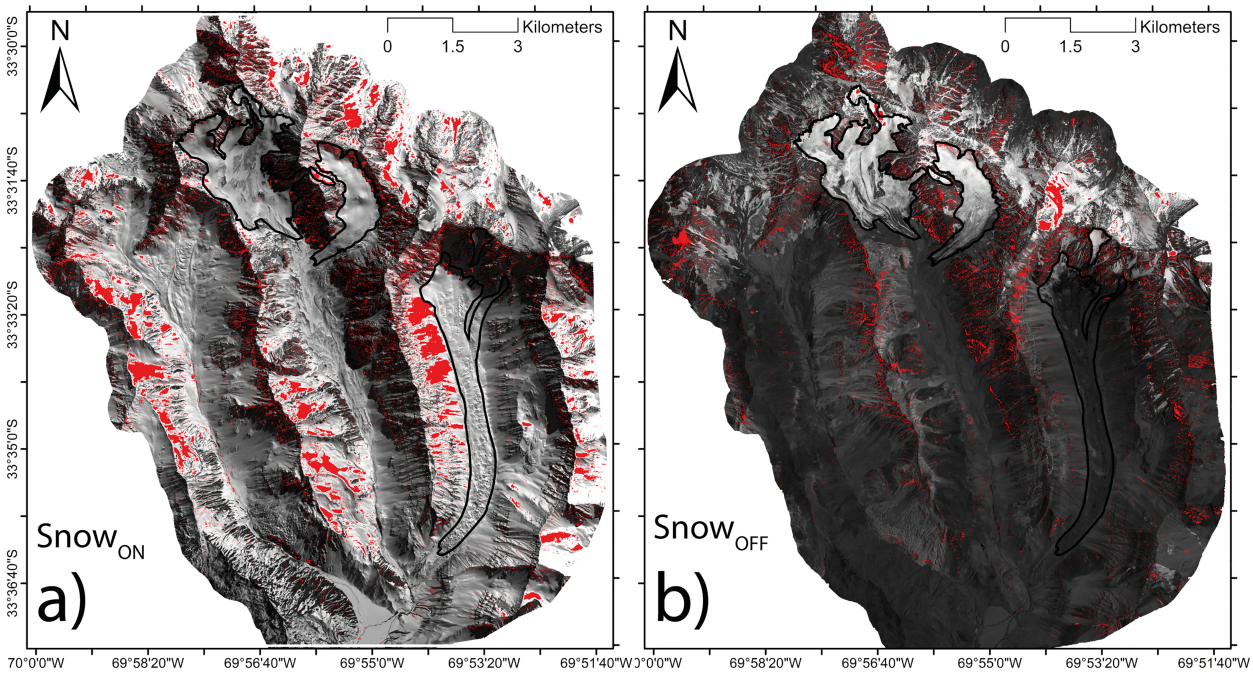

Figure 2. Map of the study basin with Pléiades orthoimages for (a) Snow$_{ON}$ (04/09/2017) and (b) Snow$_{OFF}$ (06/01/2018) Red areas indicate data gaps in the respective DEM.

The PLE_Snow$_{ON}$ acquisitions were on 4 September 2017, and the PLE_Snow$_{OFF}$ acquisitions were on 6 January 2018, capturing a total area of 136 km^2 (Figure 2). The high solar angles for the austral summer resulted in zero shadowing for the PLE_Snow$_{OFF}$ imagery, though topographic shadowing is present in ~10% of the PLE_Snow$_{ON}$ imagery on slopes of a southwest orientation (Figure 2a). Additionally, failure of image correlation produced gaps in the PLE_Snow$_{ON}$ DEM for areas of high image saturation (dominant for steep, east-facing slopes, equivalent to ~5% of the study area). We note that early snowfall during the Autumn of 2017 (April-May) restricted acquisition of PLE_Snow$_{OFF}$ images prior to the PLE_Snow$_{ON}$ images, and thus, vertical differencing with a PLE_Snow$_{OFF}$ acquisition during January 2018 includes some horizontal and vertical motion, surface lowering from glacier ablation and firn densification in glaciated areas (Belart et al., 2017). Accordingly, the Pléiades snow depth map cannot represent accurate snow depth variations over the glaciers in the study catchment and are corrected with ground-based information to address aim 2 (see section 3.6). An uncorrected vertical differencing of these DEMs forms the original snow depth estimate, hereafter referred to as Pléiades$_{ORIG}$. The nomenclature of this and all apparent snow depth maps mentioned in this work (see section 3.6) are given in Table 1.

Table 1
A Summary of the Main Acronyms Used in This Study

Item	Description	Date (if applicable)
Pléiades$_{ORIG}$	Processed DEM difference in ASP (apparent snow depth) without corrections or filters.	04/09/2017–06/01/2018
Pléiades$_{REG}$	Co-registered to a local LiDAR DEM- Filtered based upon snow holding capacity	04/09/2017–06/01/2018
Pléiades$_{GLA}$	Glacier-corrected snow depth map	04/09/2017–06/01/2018
Pléiades$_{SR}$	Snow removal based upon multispectral image classification	04/09/2017–06/01/2018
Pléiades$_{CORR}$	Final product after gap filling from random forest model	04/09/2017–06/01/2018
Planet$_{GLA}$	Planet image to correct for glacier dynamics	14/04/2017
Planet$_{SR}$	Planet image to remove snow in TOPO and DBSM estimates	07/09/2017
TOPO	Multiple regression model for predicting snow depth based upon topographic parameters	04/09/2017
DBSM	Distributed blowing snow (energy balance) model with or without snow redistribution	04/09/2017

Note. As a verification, the relative registration vector between both Pléiades DEM (v3) was also estimated for horizontal shifts and compared in the bottom row. Further vertical shifts of Snow$_{ON}$ are described in the text.

Table 2
Components of the Translation Vector That was Found to Optimize the Registration of the Pléiades DEMs on the Reference LiDAR DEM

Name	Source DEM	Reference DEM	shift in E/W (m)	shift in N/S (m)
v1	Pléiades $Snow_{ON}$	LiDAR $Snow_{OFF}$	−10.19	−10.74
v2	Pléiades $Snow_{OFF}$	LiDAR $Snow_{OFF}$	−10.16	−1.06
v3	Pléiades $Snow_{ON}$	Pléiades $Snow_{OFF}$	−0.89	−9.59
v3-v2-v1	-	-	0.86	−0.09

3.4. PlanetScope Images

We obtained two 3 m PlanetScope images (PlanetTeam, 2018) to aid our analyses. One image was obtained 14 April, before the arrival of the 2017 snow season, to benefit corrections to glacier motion (see section 3.6). The second is an image obtained as close to the PLE_Snow_{ON} acquisition as possible (7 September 2017), used to identify snow-free areas for the alternative model estimations (see section 3.7). We refer to these PlanetScope images as $Planet_{GLA}$ and $Planet_{SR}$, respectively. Due to a 10 m geolocation error (Cooley et al., 2017), we georeference each PlanetScope image onto our PLE_Snow_{OFF} orthoimage using visible tie points.

3.5. Topographic Parameters

We calculate the following topographical parameters from the PLE_Snow_{OFF} DEM of the Pléiades acquisitions (section 3.3): (i) Slope (SLP), (ii) Northness (NOR), calculated here as aspect relative to south (such that 180° = north), (iii) a topographic position index (TPI) that is considered as the relative elevation of a cell compared to its neighborhood cells, (iv) the cell exposure parameter (Sx) used as a proxy for wind effects on snow (re)distribution (Winstral et al., 2002), and (v) a visible sky view factor (SVF), calculated using the SAGA GIS function of the same name. We note that the value of NOR is the inverse of that published by previous work (e.g., Grünewald et al., 2013) due to the study site's location in the southern hemisphere (180 - abs(360 - Aspect >180)). The Sx parameter is calculated using the modal direction of wind derived from 1979–2017 ERA Interim (*Dee et al., 2011*) u and v 10 m wind components, which in this region equals 268°. This is corroborated with information at the Termas del Plomo (TdP) AWS records during 2017 in the lower section of the catchment (Figure 1c). We apply an Sx search distance of 200 m and a TPI search range of 60 m, which was found to have the highest Pearson's partial correlation with snow depth of the registered Pléiades images ($Pléiades_{REG}$—section 3.3). Including the cell elevation itself directly from the DEM, we use a total of six parameters for the catchment for our analyses. For model estimations of distributed snow depth (see section 3.7), we additionally calculate these topographical parameters from an independent 30 m ASTER (Advanced Spaceborne Thermal Emission and Reflection Radiometer) GDEM. This was performed to compare Pléiades snow depths to alternatives that are completely independent of Pléiades-derived data.

3.6. Correction of Pléiades Snow Depths

3.6.1. Co-registration of Pléiades

Because we want to compare the Pléiades snow depths with the LiDAR snow depths, we need to register the Pléiades DEM to the same absolute reference as the LiDAR. Hence we computed the horizontal shift between the PLE_Snow_{OFF} DEM and the LiD_Snow_{OFF} DEM (registration pair v1—Table 2). This was done by minimizing the standard deviation of the elevation differences between both DEMs in non-glacierized areas with slopes higher than 4° and lower than 60° (Berthier et al., 2007). To check the results of this optimization, we apply the same method to co-register the PLE_Snow_{ON} DEM to the LID_Snow_{OFF} DEM (registration pair v2) for the entire domain. We obtain an independent estimate of the relative co-registration between both Pléiades DEMs for this subdomain only (registration pair v3), which is found to be consistent with the absolute shift between Pléiades DEMs and the LiDAR DEM (v1-v2 ~ = v3, Table 2, Figure 3). We note that the transformation to horizontally register the Pléiades DEMs was restricted to a translation (shift in the XY plane) and comparable to the approach of Nuth and Kaab (2011). The difference between both methods is given by the norm||v3-v3Nuth&Kääb|| = 0.62 m, which is 15% of the pixel size. For an analysis of error, we checked that v1-v2 is equivalent to v3 by computing the norm of the vector v1-v2-v3. We found||v1-v2-v3||= 0.36 m, indicating that the LID_Snow_{ON} DEM is sufficient to align each 4 m Pléiades DEM on this reference (Table 2).

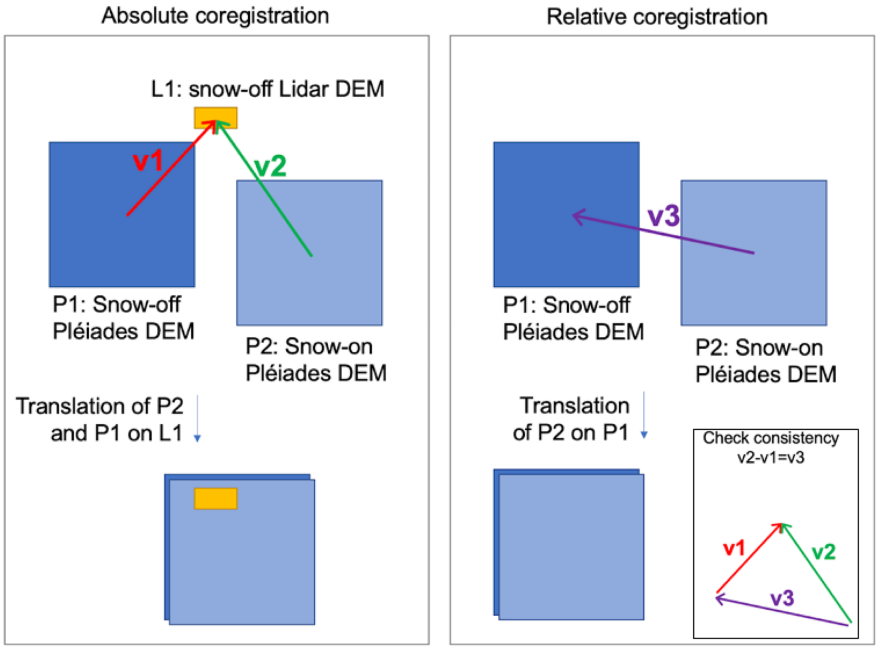

Figure 3. A schematic of the method applied to evaluate the robustness of the absolute co-registration on the LiDAR DEM.

The vertical registration between the PLE_Snow$_{ON}$ and the PLE_Snow$_{OFF}$ DEMs was calculated from the elevation difference for bare rock areas in the PLE_Snow$_{ON}$ orthoimage of the nadir acquisition (corresponding to the stable areas, i.e., where elevation difference should be zero). Snow free areas of the PLE_Snow$_{ON}$ nadir orthoimage were classified using a Gaussian mixture model trained on 50% of a total of 2.9 * 10^5 samples of the following classes: snow-free (bare rock), snow-covered, shaded snow, and bare ice. The whole image was classified in QGIS using the Dzetsaka plugin v3.4.4 (Karasiak, 2019), and the remaining 50% of the samples were used to evaluate the classification using Cohen's kappa. We obtained a kappa of 0.95, indicating a strong agreement.

The median value of the sampled bare rock values (−0.70 m) was used to vertically shift the PLE_Snow$_{ON}$ DEM so that the median elevation difference is zero over these snow-free areas. We utilize three standard deviations of the normalized median absolute deviation (NMAD) of difference over snow free surfaces to limit extreme outliers in co-registration process that are associated with high slope angles (>60°). This method is identical to the one used by Marti et al. (2016) except that in that case the vertical shift was estimated on a single snow free area (a football field). In the study area, there is not such a flat snow-free target; therefore, we used snow free patches across the image where snow did not accumulate due to wind effects or remain due to radiation forcing.

We finalize these initial corrections by limiting the slope dependent snow holding capacity of the entire Pléiades domain based upon the relation presented in Figure 2 of Bernhardt and Schulz (2010), in order to remove extreme outliers for steep slopes. This snow depth map is hereafter referred to as Pléiades$_{REG}$ (Table 1).

3.6.2. Snow Depth Comparison With LiDAR

For a comparison of Pléiades and LiDAR snow depths, we subsampled the Pléiades$_{REG}$ map to a bounding box of the scan domain and cubically resampled the LiDAR snow depth map to 4 m. We consider the LiDAR depths as our "reference" dataset (such that the snow depth difference is calculated as Pléiades − LiDAR). We note that we use the LiDAR here as the best available source for comparison of elevations from the Pléiades data, though this information is not available as a fully distributed dataset (e.g., Bagnardi et al., 2016; Zhou et al., 2015). Additionally, due to the nine day temporal offset between LiDAR and Pléiades acquisitions, we calculate a mean 0.03 m (±0.005) of surface lowering (equal to 0.018 m w.e. melt) using the energy balance routine of a distributed blowing snow model

(as described in section 3.7.2). We thus add the calculated amount of melted snow to the snow-covered areas of the LiDAR snow depth map (we note that we do not add the snow depth to snow-free areas of the LiDAR snow depth map). Following relative co-registration of Pléiades DEMs, median differences over snow-free terrain are set to zero (section 3.6.1). However, DEM double difference (Pléiades apparent snow depths minus that of the LiDAR) over snow free areas in a subdomain is not necessarily with a median of zero, and thus we remove any vertical bias in the two to provide a more direct comparison.

Following Marti et al. (2016), we assess the quality of the Pléiades snow depth map in comparison to the LiDAR using the mean and the median to evaluate the vertical accuracy, and the standard deviation and the normalized median absolute deviation (NMAD) to calculate vertical precision and provide an estimate of random error of Pléiades.

3.6.3. Adjustment of Glacier Snow Depths

To improve the representation of snow depth over the glaciers, we adjust the surface for (i) horizontal and vertical motion, (ii) vertical emergence, and (iii) ice ablation. The details of this process are given in the supporting information and only summarized here. Horizontal and vertical motion is corrected for the PLE_Snow_{OFF} DEM by spline interpolation in ArcGIS using crevasses and clear surface features as tie points in the PLE_Snow_{OFF} orthoimage and $Planet_{GLA}$ (assuming minimal motion during the winter months). Along-glacier vertical ice emergence was calculated using the flux gate method of Vincent et al. (2016) and Brun et al. (2018) in 100 m elevation intervals. We obtain ice thickness from ground penetrating radar measurements (Rivera, 2012) and calculate the ice flux and uncertainties following Brun et al. (2018). The relative contribution of ice ablation to the total ablation between October 2017 and January 2018 was modeled assuming that there was no difference in the snow coverage between the PLE_Snow_{ON} acquisition (September 2017) and the date of probe measurements of snow depth (October 2017). Spatially interpolated probe depths on the glaciers (section 3.2) were used to initialize a distributed energy balance model based upon Ayala et al. (2017) to calculate the total amount ice ablation across the glacier, forced by temporary on-glacier AWSs and validated against distributed ablation stakes (Figure 1). Quantities of ice ablation (converted to a surface height change based upon measured snow density and the assumed 900 kg m^3 density of ice) were added to the PLE_Snow_{OFF} DEM in order reduce snow depths for areas associated with subsequent ice ablation. The differences between the original and corrected PLE_Snow_{OFF} DEMs were used to make the correction to the $Pléiades_{REG}$ snow depth map (Figure S2). Propagating error throughout these steps results in an uncertainty of ~30% for the glaciers of this catchment. Finally, for each glacier, we set snow depth to zero if it was classified as bare ice in the Gaussian mixture model of the PLE_Snow_{ON} orthoimage, regardless of any previous changes described. For example, snow removal from wind scouring is a common occurrence on Bello Glacier. This glacier-corrected snow depth map is referred to as $Pléiades_{GLA}$ (Table 1).

3.6.4. Gap Filling Spatial Snow Depths

We correct low (< 0.01 m) or negative values of $Pléiades_{GLA}$ by identifying snow-free areas (zero "snow depths") from the PLE_Snow_{ON} orthoimage by using the Gaussian mixture model described in section 3.6.1. This step of the correction process is referred to henceforth as "$Pléiades_{SR}$" (Table 1).

The snow depth map at this stage required gap-filling to provide a spatially complete estimate of snow depths. We explore the relationship of the $Pléiades_{SR}$ snow depth map with topographical parameters as described in section 3.5, using a Random Forest model (Breiman, 2001), initiated with 100 individual regression trees. The importance of each predictor is assessed by permuting each one in turn using the "out-of-bag" test dataset whilst keeping others unchanged (see López-Moreno et al., 2017 for details). Utilizing the whole dataset except the glacierized areas, we use the model predictions of snow depth to fill the remaining missing values that exist in the $Pléiades_{SR}$ snow depth map. We adjust the gap filled data using the regression relationship between the estimates of the random forest model and the observations ($Pléiades_{SR}$). This final form of the apparent snow depth map is referred to as $Pléiades_{CORR}$ (Table 1).

3.7. Alternative Model Estimations of Snow Depth

To highlight the potential utility of the Pléiades for deriving snow depth at high elevation (within the entire catchment), we compare $Pléiades_{CORR}$ snow depths to two models of snow depth estimation

from the literature (as detailed in the following subsections) at a spatial resolution of 30 m and using the ASTER GDEM for elevation information (section 3.5). It should be stressed that we do not utilize the full potential of these alternative model approaches, in the sense that we do not use the Pléiades data itself for any calibration, under the assumption that we have no distributed data available for the catchment. For each model approach described in the following subsections, we additionally set snow depths to zero based upon bare rock areas classified from the Planet_{SR} image (section 3.4).

3.7.1. Statistical Estimation Using Topography (TOPO)

We apply a statistical estimation of snow depth based upon the topographical information provided in section 3.5 and independent coefficients derived from "global" datasets of glacierized and non-glacierized catchments (Table 4 of Grünewald et al., 2013). These coefficients were derived from 10 LiDAR datasets of seven basins in Europe and Canada to generate a regression equation of relative snow depth (rSD):

$$\text{rSD} = 0.00079 \cdot \text{rDEM} - 0.0145 \cdot \text{SLP} - 0.0028 \cdot \text{NOR} + 0.28, \quad (1)$$

where the rDEM is the relative elevation of the catchment, taken as the ASTER GDEM elevation minus the mean (3930 m a.s.l.) and NOR remains unaltered due our inversion of values based upon the southern hemisphere (see section 3.5). As rSD was modeled for multiple study sites of varying snow depths in Grünewald et al. (2013), we add the mean value of all manual measurements in September and October (section 3.2) to derive an absolute snow depth (hereafter "TOPO"), in absence of other measured data. This value is equal to 1.57 m, similar to the mean value of Pléiades_{ORIG} (see section 4.1).

3.7.2. Snow Redistribution by Wind Model (DBSM_{WIND})

We use hourly precipitation records at the Yeso Embalse (YE) AWS (section 2, Figure 1b) and other energy balance variables at TdP (Figure 1c) from 4 March to 4 September 2017 to force the distributed blowing snow model (DBSM) developed by Essery et al. (1999). The model requires hourly air temperature, relative humidity, incoming radiation, wind speed and direction and precipitation as inputs to calculate the gridded energy balance and the sublimation/transportation of snow by wind. We distributed precipitation across the catchment using a positive logarithmic gradient, as suggested by Burger, Brock, and Montecinos, (2018) for meteorological stations in the Maipo catchment (2000–2015), although locally calibrated based upon 2017 precipitation records at TdP AWS. The precipitation P (mm) for time step t, at elevation z was prescribed by:

$$P(t,z) = P_{YE}(t) \cdot (0.686 \cdot log\,(z) - 2.014), \quad (2)$$

where P_{YE} is the hourly record of precipitation at YE AWS.

Snow was accumulated assuming a solid precipitation threshold of 1 °C (Ayala et al., 2016), and air temperature was distributed using an environmental lapse rate from TdP AWS (−0.0065 °C m^{-1}). Data for incoming radiation and relative humidity were assumed to be spatially constant, though net fluxes are adjusted using calculated albedo evolution and surface temperatures for each time step of the model (see Best et al., 2011 for details). Normalized wind maps (relative to wind speeds recorded at TdP) for an 8-point compass direction are computed using the Mason and Sykes (1979) model, which solves linearized momentum equations through Fourier transforms of bare earth topography. However, to preserve the assumption of low terrain slopes (for which this method was developed), we smooth the topography of the ASTER GDEM by a factor of 1.4. This was based on numerical experiments conducted at the Izas experimental catchment (Revuelto et al., 2014; Revuelto et al., 2017), for which good results were obtained when comparing with LiDAR observations near the maximum accumulation date (not shown). We find a good agreement between the modeled snow depths for 14:00 Coordinated Universal Time (UTC) on the 13 September in the lower catchment when comparing to the LiDAR snow depths (mean, median and standard deviation of differences = 0.03, 0.04, and 0.14 m, respectively), suggesting that the model may realistically reproduce physical processes of the lower catchment. The distributed snow depth at 14:00 UTC on 4 September 2017 is presented for comparison with Pléiades, hereafter referred to as "DBSM_{WIND}."

3.7.3. Excluding Wind Transportation (DBSM_{NoWIND})

We present another case by using the model and meteorological forcing and distribution described in section 3.7.2, though neglecting snow transportation by wind (hereafter "DBSM_{NoWIND}").

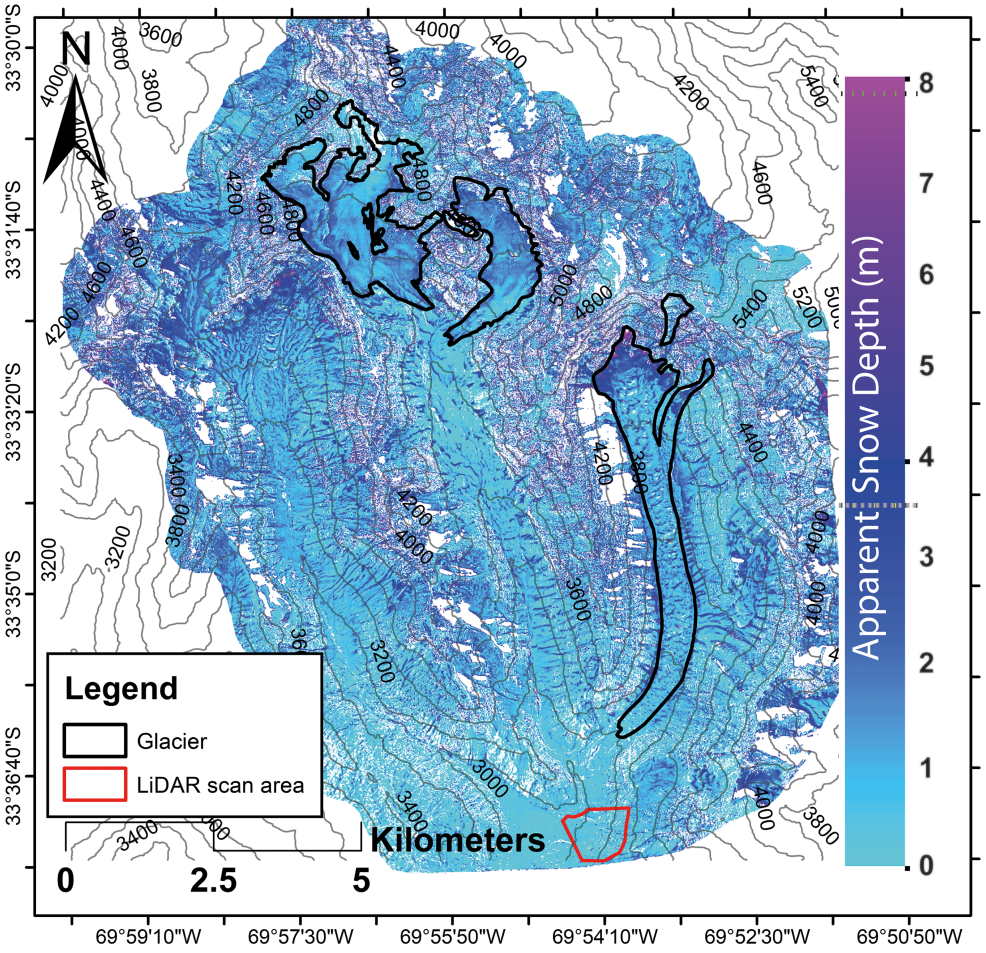

Figure 4. The elevation difference of DEMs or "apparent" snow depth map (m) of $Pléaides_{ORIG}$. The map displays a 4 m product with a color scale between 0 (light blue) and 8 m (purple).

4. Results

4.1. Raw Pléiades Snow Depth

Figure 4 shows the raw output of the Pléiades DEM vertical differencing ($Pléiades_{ORIG}$—Table 1) for the Rio del Yeso basin. The mean, median and standard deviation of snow depths of $Pléiades_{ORIG}$ are 1.66, 1.07, and 0.26 m, respectively. Approximately 17% of the total survey area has missing data, predominantly as result of image saturation on the east-facing slopes of the valleys. We find that ~12% of the data provide negative differencing values (mean of negative values = −0.26 m) where snow is thin or patchy, typically in pro-glacial regions and at lower elevations. Further still, for high slope angles and intervalley ridges of the basin, poor registration of the stereo triplets results in sporadic patterns of missing values and high vertical differences (exceeding 6 m—Figure 5) which do not correspond consistently to the presence of snow visible from the Pléiades orthoimages (Figure 2). Thus, an additional 2.5% of the dataset exceeds 6 m of "apparent snow depth" (Figure 4), around two thirds of which exist on slopes >30°. Importantly, the summation of these effects results in almost one third of the Pléiades acquisition (~43 km^2) which lacks "usable" data as an "end-product." Visually, $Pléiades_{ORIG}$ is able to resolve many local features, such as avalanches, small channel infilling, and valley troughs, revealing a nonlinear relationship between snow depth and elevation in the basin (Figure 5a). For example, within the pro-glacial region of the central valley (Figure 4), snow cover is limited and often thinner than that lower in the valley (typical elevation differences of this subarea ranging from −0.30 to 0.70 m). The snow depth data otherwise display a gamma distribution (Figure 5b), in agreement with previous studies (Marti et al., 2016; Winstral & Marks, 2014), with ~47% of the total snow depth values being between 0 and 2 m.

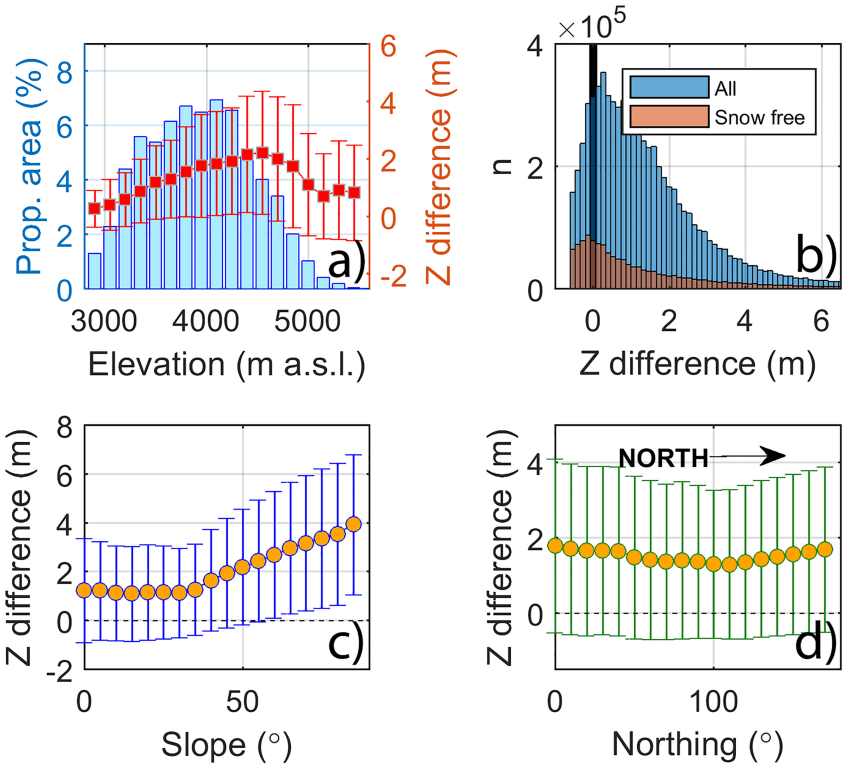

Figure 5. (a) The elevation vs "snow depth" relationship for $Pléiades_{ORIG}$. The error bars represent the standard deviation of apparent vertical (Z) difference for each 150 m elevation band. The left hand axis represents the proportional area of each 150 m elevation band as a percentage of the total. (blue bars). (b) Histogram of vertical differences of PléiadesORIG for all cells as those classified as snow free from the Gaussian mixture model (red). Panels (c) and (d) show the relationship of mean vertical differences for snow free cells against slope angle (5 degree interval) and northness (10 degree intervals), respectively.

4.2. Ground-Based Evaluation

Snow depth probes provide a good agreement with the 0.5 m LiDAR snow depth map at the scanning subdomain ($R^2 = 0.65$, RMSE = 0.32 m) and give confidence to the validity of the LiDAR measurements used as our reference dataset (Figures 6a and 6c). Snow depths are generally small at this site, which is at low elevation and northwest orientated.

Mean and median differences of LiDAR snow depths and $Pléiades_{REG}$ (section 3.6.2) are −0.10 and −0.22 m, respectively, and standard deviation of differences and NMAD are 0.21 and 0.36 m, respectively. The root mean square error (RMSE) of the two products is found to be 0.52 m. These differences are smallest for flatter terrain (Figures 6e and 6f, Figure 7), and largely within the range of error of Pléiades and the LiDAR observations (nondelineated areas of Figure 7b) and produce a normal distribution of errors with a negative bias (Figure 7a). Within troughs and on higher slope angles, snow depth differences are positive, indicating an over-estimation by $Pléiades_{REG}$ (Figures 6b and 6f and Figures 7b and 7c). However, $Pléiades_{REG}$ produces shallower snow depths in comparison to the LiDAR dataset on average, especially for south facing slopes (Figure 7d), likely as a result of shadowing. Visual inspection of Figures 6a and 6b reveal that Pléiades is able to capture the general patterns of snow depth variability, though is subject to a larger degree of noise. We note that slight jitter effects were detected in the Pléiades acquisition of this basin (Most notably for the PLE_SnowOFF image acquisition) but lower than the error due to radiometric noise in the shaded slopes (Figures 4 and S1).

Additionally, increases in the median snow depth following vertical registration of Pléiades largely solves the problem of negative snow depths prevalent in the $Pléiades_{ORIG}$ dataset (section 4.1). Comparison of $Pléiades_{REG}$ and the LiDAR snow depths (Figure 7b) reveal a visible relation to the northness (NOR) of

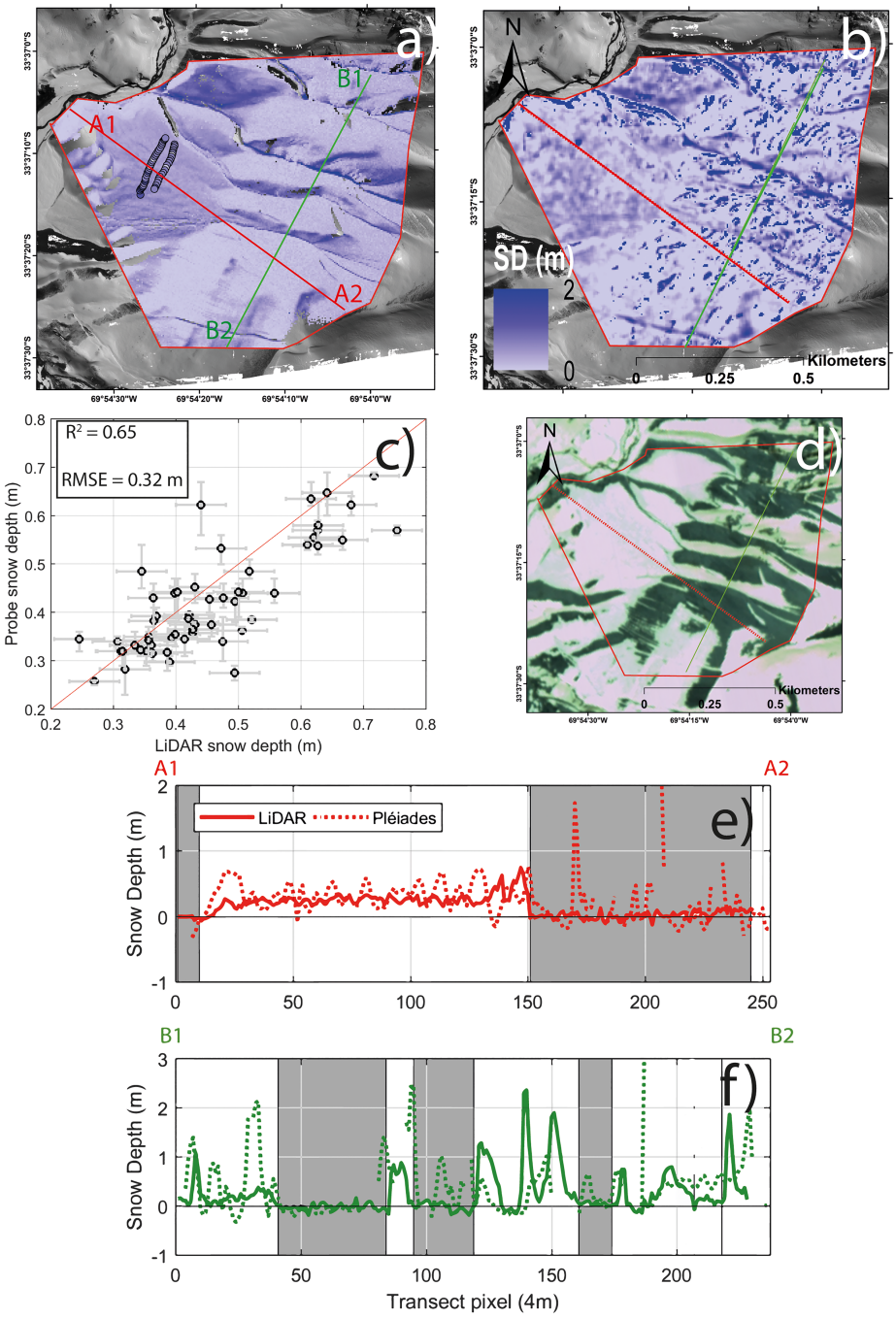

Figure 6. Maps of LiDAR (a) and Pléiades (b) derived snow depths for the LiDAR subdomain (scale bar identical capped at 2 m). Panel (a) also shows the position of manual probe snow depths and arbitrarily defined transects for comparison of Pléiades and the LIDAR snow depths. Panel (c) compares the LiDAR "reference" dataset to the probe depths and (d) shows the snow free areas at the time of LiDAR acquisition ($Planet_{SR}$). Panels (e) and (f) show the comparison of $Pléiades_{REG}$ and LiDAR snow depths along the defined transects A1-A2 and B1-B2, respectively. The shaded areas denote snow-free areas. In (c), the vertical error bars represent the range of recorded probe snow depths at each point and the horizontal error bars represent the mean 0.08 m uncertainty calculated for the LiDAR acquisitions

the LiDAR subdomain (Figure 7d), though this relationship is weak (R^2 = 0.05) and is likely not representative of the entire catchment (Figure 5d), thus no correction was applied here. Furthermore, we do not find any noteworthy relation between LiDAR incidence angle and the differences in snow depth products here (e.g., Currier et al., 2019).

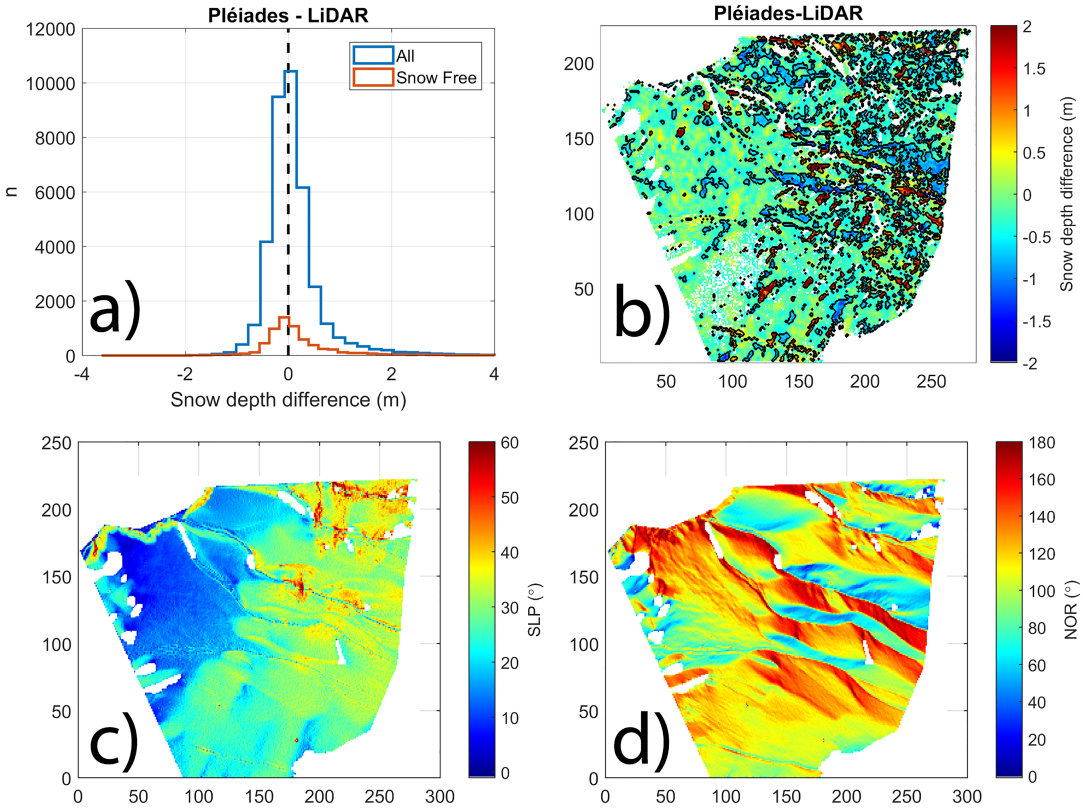

Figure 7. (a) Histogram of snow depth difference ($Pléiades_{REG}$-LiDAR) including 0 difference line (black dashed line) and median difference of all pixels (red dashed line). (b) The $Pléiades_{REG}$ snow depth compared with the LiDAR ($Pléiades_{REG}$-LiDAR). Differences greater than the propagated error of both datasets (0.533 m) are shown by the black outlined areas. Under-estimation of the $Pléiades_{REG}$ compared to the LiDAR is shown in blue (negative values). Panels (c) and (d) show the slope angles (SLP) and northness values (NOR), respectively. NOR values closer to 180 indicate a north facing slopes.

4.3. Correction to Pléiades Snow Depths

The following subsections present the results of the evaluation of Pléiades snow depths against the LiDAR measurements and subsequent corrections to the $Pléiades_{REG}$ snow depth map. Figure 8 shows the overview of the changes at each step for a subdomain of the Pléiades acquisition, with changes to the elevation-average snow depth at each step shown in Figure 8e.

4.3.1. Snow Depth Over Glaciers

Prior to any correction, mean and standard deviation of $Pléiades_{REG}$ for the glacier areas was 1.46 and 1.20 m, respectively. After correction for motion, emergence and ice ablation (see supplementary material), glacier mean and standard deviations of snow depth were 1.34 and 0.98 m, respectively. The largest changes were found for Bello Glacier, which lost 33.5 ± 9% of snow volume, notably adjusting the glacier snow depths to show an inverse relationship with elevation (Figure 8b), consistent with trends of the snow probe observations. Yeso and Piramide glaciers, respectively, lost 9.3 ± 2.8 and 30.1 ± 9% of snow volume following this correction. The difference in total catchment snow volume following the correction for glacier surfaces ($Pléiades_{GLA}$ − $Pléiades_{REG}$) was −4.7 ± 1.4% (Figure 8). The combined uncertainty of corrections for vertical velocity and ice ablation resulted in mean differences of 0.06 m (max 0.13 m) in the final calculated snow depths over the glaciers.

4.3.2. Correction of Negative and Missing Pléiades Snow Depths

The Gaussian mixture model (as described in section 3.6.1) was applied to set the identified snow-free areas of the $Pléiades_{GLA}$ snow depth map to zero. A correction of 35% of snow map's pixels using this approach resulted in ~10% snow volume loss for $Pléiades_{SR}$ compared to $Pléiades_{GLA}$ (6c).

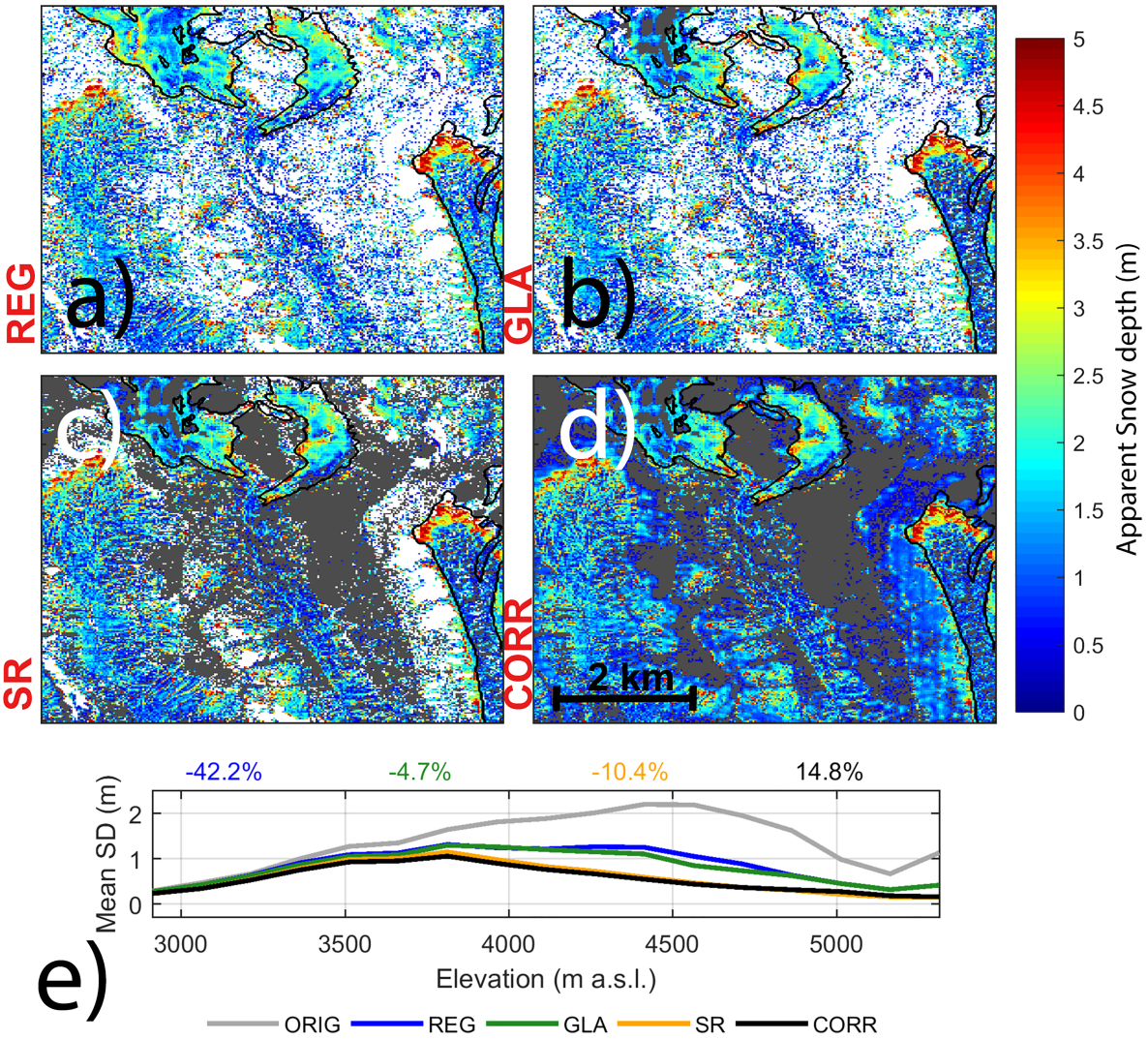

Figure 8. Maps of the Pléiades apparent snow depth correction process (focused upon a subdomain for clarity), where (a) is $\text{Pléiades}_{\text{REG}}$ (after horizontal registration, vertical offset and removal of extremes), (b) is PléiadesGLA (after correction for glacier dynamics and ablation), (c) is PléiadesSR (after classification of zero snow areas) and (d) is PléiadesCORR (the final corrected snow depth map after gap-filling from the random forest model). White areas denote missing data and dark gray areas denote zero snow. Panel (e) shows the elevation-mean snow for each map, with percentage change compared to the previous step shown by the colored values above.

A random forest model was applied to fill remaining gaps of the $\text{Pléiades}_{\text{SR}}$ snow depth map. The model results show that elevation is the most influential variable for predicting snow depth in the entire Rio del Yeso basin, followed by NOR and Sx (Figure 9). TPI, SLP and SVF are found to be less influential in the predictor skill of the Random Forest approach. Figure 9a shows the observed $\text{Pléaides}_{\text{SR}}$ snow depths against the estimated values of the random forest model. The results show a skew of over-estimation for shallow snow depths and under-estimation for the deepest snow areas (i.e., avalanche deposits). In general, the model adjustment capability is good ($R^2 = 0.76$), and although is over-fit to the data in this instance, presents a useful means of gap filling where interactions between independent topographical variables are also considered (López-Moreno et al., 2017). The mean and standard deviation of the gap filled snow depths were 0.84 and 0.32 m, respectively. Through gap-filling, total volume of snow was increased by 14.8% compared to $\text{Pléiades}_{\text{SR}}$, though elevation-mean snow depths remained similar (Figure 8e).

4.4. Comparison of Model-Derived Snow Depth With Pléiades Snow Depth

Figure 10 displays the snow depths of $\text{Pléiades}_{\text{CORR}}$ and the models approaches described in section 3.7 at a horizontal resolution of 30 m, with descriptive statistics of each method shown in Table 3.

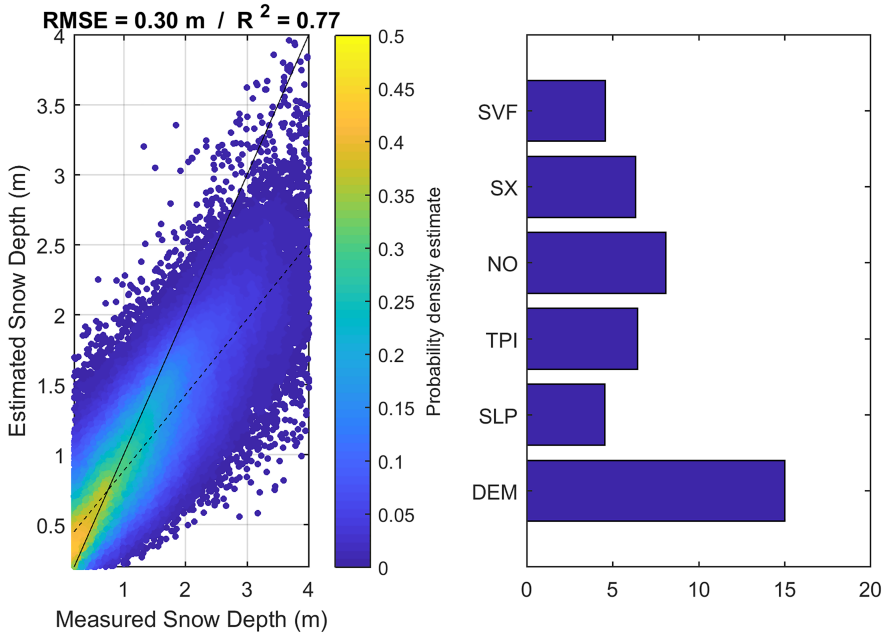

Figure 9. (a) $Pléiades_{SR}$ (x-axis) vs. Estimated (y-axis) snow depth (m) for the Rio del Yeso basin. The color-scale indicates the density of points, such that yellow is highest density of points. The regression relationship (dashed line) is used to gap fill Pléiades data to produce the $Pléiades_{CORR}$ snow depth map. (b) The delta error of the "out-of-bag" (OOB) test datasets which represent variable importance. The solid line in panel a) denotes the 1:1 line for the observed and estimated apparent snow depths for the $Pléiades_{SR}$. The left panel axes are capped at 4 m for aiding the visualization of point density (colors).

Figure 10a demonstrates the heterogeneity of snow depths and the high quantity of zero snow pixels in the basin (35% of the total $Pléiades_{CORR}$ pixels) which are distributed across the entire elevation range. Mean $Pléiades_{CORR}$ snow depths rapidly increase until ~3500 m a.s.l., steadily increase to approximately at 3900 m a.s.l., followed by a steady and continuous decline up to the highest elevations (Figure 11a) and steeper slopes (Figure 11b). Snow depths derived from TOPO (Table 1), however, display a strong reliance upon elevation, with snow depths >4600 m a.s.l. averaging 1.71 m (Figure 11a), but also reveal thin snow depths (<0.05 m) on the north slopes of the lower basin, consistent with $Pléiades_{CORR}$ (Figure 10b). However, ridges of the basin demonstrate unrealistically high snow depths outside of the error range of $Pléiades_{CORR}$. Furthermore, avalanche deposits, such as on Piramide Glacier or the western valley (Figures 2 and 4), cannot be accounted for.

$DBSM_{NoWIND}$ snow depths are governed highly by slope orientation and the control of shortwave radiation during the winter (Figures 10c and 11d). The logarithmic precipitation gradient is calibrated based upon station observations in the lower part of the basin (2975 m a.s.l.) though cannot account for the general higher accumulation or preservation of snow within concave landforms (Figure 11c) where avalanches occur and snow depths are highly heterogeneous (Figures 2a and 10a). Higher elevation snow depths exceed that of $Pléiades_{CORR}$ > 4200 m a.s.l. (Figure 11a), though does not replicate the effect of avalanches and mechanical snow removal which are the biggest causes of the low snow depths at this elevation (Figure 10c). Similarly, $DBSM_{WIND}$ snow depths strongly underestimate across the basin (Figure 10d) though notably removes snow from the exposed, convex ridges (Figure 11c) of the upper most elevations, and accumulates a lot of snow for locations with minimal SVF (Figure 11f). $DBSM_{NoWIND}$ and $DBSM_{WIND}$ show similar behavior to the observations for Sx (Figure 11e), though more as a result of solar radiation angles and the energy balance component of the DBSM model (Figure 11d) than due to wind processes.

Differences in total quantity of snow volume for TOPO, $DBSM_{NoWIND}$ and $DBSM_{WIND}$ are +54.5, +1.29 and −3.96%, respectively, relative to $Pléiades_{CORR}$ (Table 2). Considering a distributed snow density calculated from the $DBSM_{WIND}$ method, the respective differences of the TOPO, $DBSM_{NoWIND}$ and $DBSM_{WIND}$ total

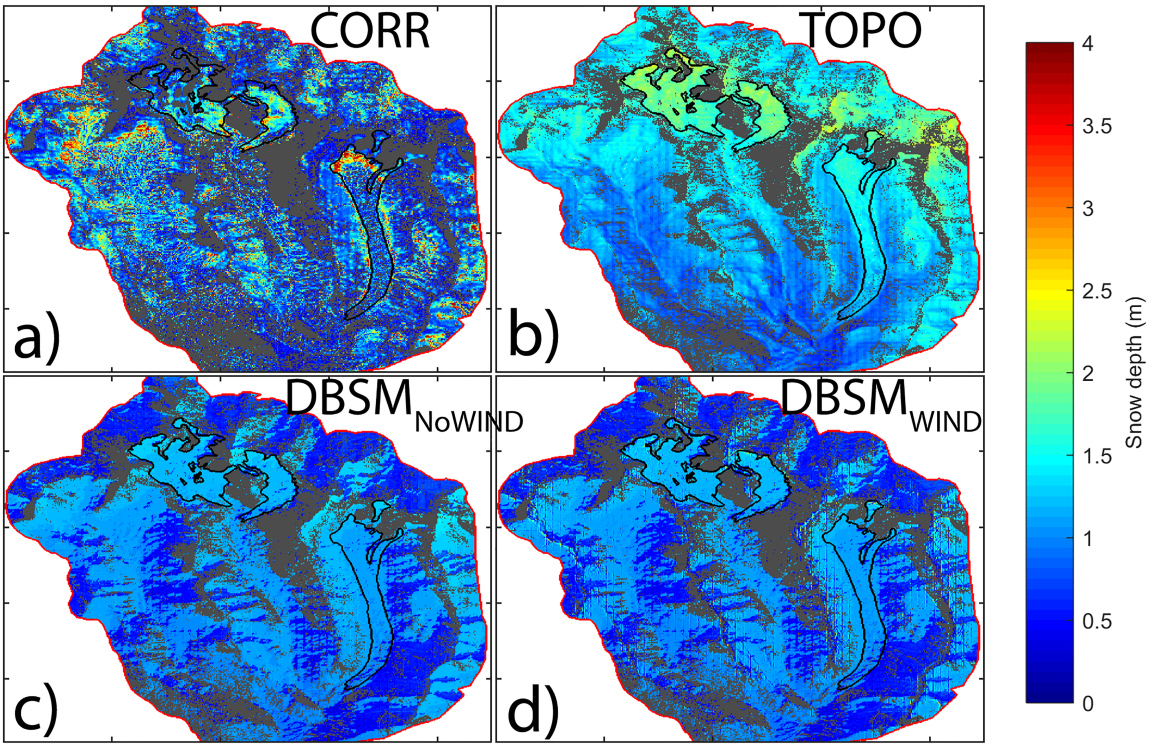

Figure 10. Observed and modeled snow depth values provided for the Rio del Yeso catchment (30 m resolution) by (a) $Pléiades_{CORR}$, (b) topographic estimation (TOPO), (c) Extrapolation of precipitation and temperature for a DBSM model run ($DBSM_{NoWIND}$) and (d) as (c) but including wind transportation ($DBSM_{WIND}$)

basin water equivalent volume are $+22 * 10^5$, $+14 * 10^5$, and $-9 * 10^5$ mm w.e. We find similar differences between the methods if snow depths over the glaciers are ignored (dashed black line in Figure 11a).

To ensure that we are not biasing the results of the Pléiades with information that could be available for the alternative estimations, we also present results of TOPO, $DBSM_{NoWIND}$, and $DBSM_{WIND}$ with removal of snow free areas visible from the $Planet_{SR}$ image (as shown in Figure 10). Evidence from supplementary Figure S3 (dashed lines) suggests that this approach allows all three model estimation methods to more appropriately represent the relationship of higher slopes (panel b), exposure to wind effects (panel e) and relation to sky view fraction (panel f). However, it is clear that neither method can replicate the dependency of snow depth with elevation though aided by high-resolution optical imagery, even if largely within the bulk error limits of the Pléiades (panel a). Figure 10 further emphasizes that mean values can sometimes be misleading and that all estimation methods fail to replicate the observations. In this case, the TOPO, $DBSM_{NoWIND}$, and $DBSM_{WIND}$ methods differ in total snow volume by +13.1, −24.6, and −28.2%, respectively, compared to $Pléiades_{CORR}$ (Table 3).

Table 3
Descriptive Statistics of Original and Corrected Pléiades Snow Depth Maps in Comparison to Alternative Model Estimations Based Upon the Literature (See Text for Acronyms)

	CORR	ORIG	TOPO	$DBSM_{noWind}$	$DBSM_{Wind}$
MEAN (m)	0.88	1.66	1.28 (0.97)	0.83 (0.64)	0.78 (0.61)
STD (m)	0.20	0.26	0.08 (0.10)	0.02 (0.04)	0.07 (0.05)
MED (m)	0.56	1.07	1.22 (1.09)	0.97 (0.70)	0.88 (0.56)
MAX (m)	7.99	55.35	2.91 (2.78)	1.54 (1.54)	7.15 (5.10)
MIN (m)	0	−30.64	0.13 (0)	0 (0)	0 (0)
Vol Diff (%)	-	+21.61	+54.5 (+13.10)	+1.29 (−24.66)	−3.96 (−28.26)

Note. Values in parentheses are considering removal of snow using PlanetScope imagery ($Planet_{SR}$).

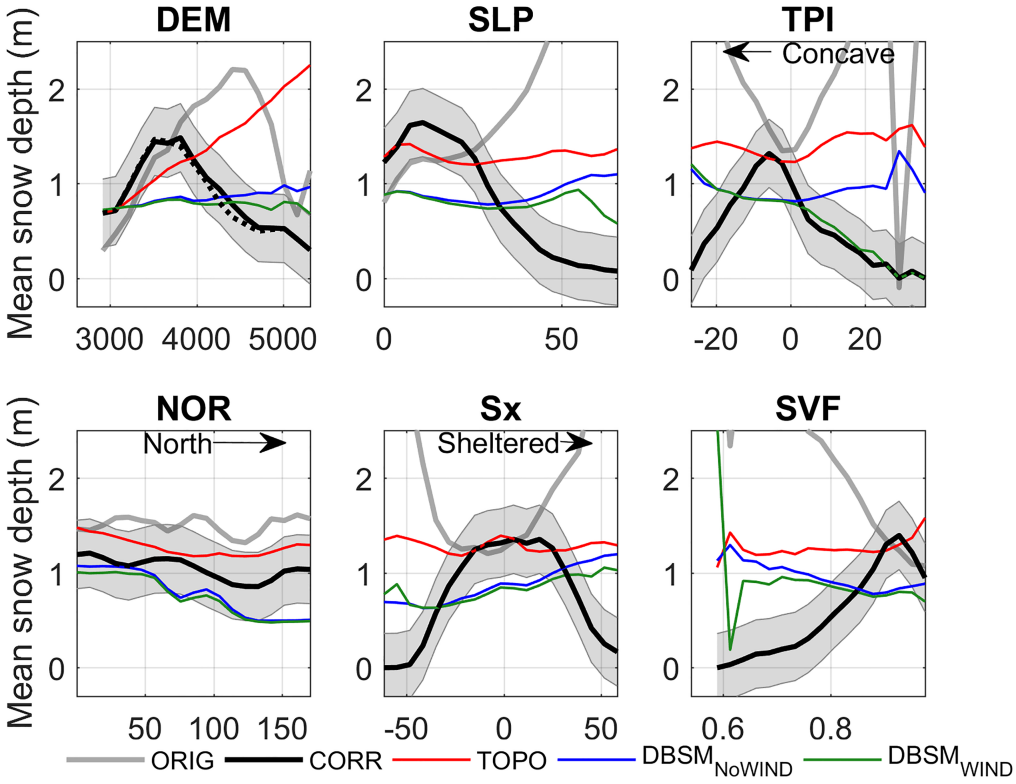

Figure 11. Mean snow depth estimated across the topographic predictors, elevation (a), slope angle (b), topographic position index (c), northness (d), wind exposure (e), and sky view fraction (f). The shaded area of $Pléiades_{CORR}$ ("CORR") indicates the 0.36 m Pléiades error of snow depth. The dashed black line (distinguishable only in panel (a) indicates where the glacier areas were ignored.

5. Discussion

5.1. Applicability of Pléiades in Central Chile

Following recent trends toward prolonged drought in central Chile (Garreaud et al., 2017, 2019) and the difficulty of appropriately prescribing the amount of snow accumulated at the end of winter (Burger et al., 2018; Ragettli et al., 2014), a high-resolution satellite product that can exploit the region's predominantly clear sky conditions is an attractive prospect for streamflow forecasting. Tasking two image triplets per year for glacierized basins (or one for non-glacierized basins) provides a distributed snow depth with potential horizontal resolutions ~1–4 m (Marti et al., 2016). Such a product is able to identify heterogeneous snow depth patterns at high elevations that are in general agreement with the literature for other parts of the world (e.g., Grünewald et al., 2013, 2014; McGrath et al., 2015; Zheng et al., 2016; López-Moreno et al., 2017). General evaluation of the Pléiades snow depths using ground based LiDAR observations suggests that the satellite approach can capture quantities of snow depths for open areas of lower slope angles (<30–40°), and most differences remain within the uncertainty bounds for the two methods (Figure 7b).

For the Rio del Yeso basin, the application of corrected Pléiades snow depth observations has clear advantages over the assumption of a temporally constant gradient of precipitation and snow accumulation (DBSM model approaches) as could be calibrated for the basin (Ayala et al., 2016; Burger, Ayala, et al., 2018) or using parameters which produce similar inter-basin characteristics in snow depth distribution (TOPO model) (Grünewald et al., 2013). The elevation-snow depth relationship (Figure 11a) is similar to that suggested by Grünewald et al. (2014), such that snow depth increases with elevation, followed by a decrease toward the highest parts of the basin due to the effects of slope holding capacity (Bernhard & Schulz, 2010) or wind redistribution (Winstral et al., 2002). Models that can account for both wind (re)distribution and avalanching during the winter season are rare but also dependent upon the limited observations at high elevations for calibration that may not be spatially representative. For example, $DBSM_{NoWIND}$ and $DBSM_{WIND}$

are prescribing too little snow at high elevations despite that the forcings and thresholds having been calibrated with AWS observations (e.g., equation 2) at a relatively high elevation for the region and being in coarse agreement with snow depths at the LiDAR site. Further still, local wind vectors assumed from ERA Interim and the TdP AWS cannot account for the local topographic and glacier katabatic adjustment of wind speeds in front of Bello and Yeso glaciers, which could be a cause of thin and zero snow depths observed in the Pléiades orthoimages and snow depth product at this pro-glacial zone. In fact, the application of DBSM for our $DBSM_{WIND}$ estimation is arguable in that the Mason and Sykes (1979) algorithm is suitable for smaller topographic variations and snow depths. Although adjusted with a correction factor in our case, results are only notably different to $DBSM_{NoWIND}$ simulations for inter-valley, convex ridges of the basin (Figure 11c) and do not resolve snow removal on the glaciers (Figure 2a). Additional snow removal using visibly snow-free areas from high-resolution PlanetScope imagery aids the representation of modeled snow depth for steep and exposed terrain for these methods (comparison of Figures 11 and S3), though still fails to capture the observed elevation-dependent variability for the catchment (Figures 10 and S3a).

We identify that, to the authors knowledge, no other topographic parameterizations have been explicitly given in the literature for the central Andes and included for our topographic model estimation (TOPO). Therefore, its applicability could be potentially questionable for comparison to snow depth observations derived from Pléiades DEMs here. Rigorous testing of individual models to estimate snow depth is beyond the scope of this paper, though nonetheless, this further emphasizes the current issues of this field of study and argues that the distinct information afforded by Pléiades satellites is thus a practical solution to these large unknowns.

5.2. Limitations of Approach

For this study we obtained an opportunistic data series of Pléiades triplet images to investigate high elevation snow depth variations. However, the nature of timing for both Pléiades and LiDAR data acquisitions must be accounted for when assessing the reliability of some of the information for the Rio del Yeso basin. We caution that comparison of snow depths between the Pléiades and LiDAR datasets are subject to a nine day temporal offset. However, we argue that differences are expected to be very small between these dates, supported by the lack of additional accumulation (corroborated with TdP AWS measurements and daily optical images of PlanetScope), small calculated mean snowmelt (0.018 m w.e.) and a low potential for snow redistribution given the densification and metamorphism of the snowpack at this point in the season given local climate conditions (Li & Pomeroy, 1997).

Although the $Pléiades_{ORIG}$ product (Table 1) reveals very different patterns of spatial snow depth compared to that of alternative model estimation methods (Figure 11), it requires some level of filtering or correction to produce a viable end-product for use in, for example, a hydrological modeling capacity. This is particularly noteworthy when observing irregularities of the original Pléiades snow depths in Figure 11 (i.e., high "snow depths" for steep slopes and convex terrain). We follow the methodology of Marti et al. (2016) and do not intend to develop this method further in our study. Nevertheless, the lack of available ground control points (for calibration or validation) limits our conclusions about the quality of the $Pléiades_{ORIG}$ snow depth product which shows large errors for steep sloped terrain (Figure 5).

In this study, we present the various steps undertaken to correct $Pléiades_{ORIG}$ for this purpose (Figure 8), though we recognize that there are steps specific to this case study. For example, as the PLE_Snow_{OFF} image was acquired following that of the PLE_Snow_{ON} image, it introduced uncertainties due to the dynamics of glaciers, comprising ~12% of the basin (corrections as given in the supplementary information). Although we calculate horizontal and vertical motion, emergence and calculate vertical differencing from ice ablation, we do not consider densification of the glacier firn layer which may further affect the DEM differencing of Pléiades (e.g., Sold et al., 2013). Belart et al. (2017) identify a significant sensitivity to this firn densification when analyzing glacier winter mass balance using DEM differencing from Pléiades on the Drangajökull ice cap in Iceland. In the case of the glaciers in the Rio del Yeso catchment, the uncertainties of snow metamorphism and densification are likely obscured by the greater uncertainty about snow depth underestimation from the timing of satellite acquisitions. In general the lack of high elevation ground-based snow and firn depth validation data (>4400 m a.s.l.) does not permit a definite estimation of the snow depth on these glaciers. Nevertheless, we identify that the large differences between the observations and model

estimation methods (Figure 10) are consistent when the glacier areas are ignored (Figure 11a), arguing that the uncertainty of snow depth for glacier areas does not dominate the potential importance of information that Pléiades may provide.

A clear limitation of Pléiades in our study is its inability to derive spatially consistent returns of snow depth for very steep slopes (>50°), which are naturally plentiful in the Andes Cordillera. Marti et al. (2016) found similar negative or very high differences (>15 m) for the steepest areas of their study site, confirming that the process is most applicable to flatter and open terrain. This is an underlying problem regarding the slope-dependent error of DEM differencing (Nuth & Kääb, 2011) and requires careful analysis and registration of each DEM. However, it is typical that such slope angles hold little snow as it is normally redistributed. In this study, we remove such extreme values and use a strong relationship between multiple topographic predictors (López-Moreno et al., 2017) to fill gaps (Figure 9) under the assumption that steep slopes will hold little or no snow and/or be subject to mechanical snow removal by wind or avalanching (Freudiger et al., 2017). We have high confidence in this approach because the PLE_Snow$_{ON}$ and PlanetScope orthoimages confirm such areas have a minimal snow cover. Further still, the large percentage of data gaps resulting from image saturation (Figure 2a) displayed no apparent avalanche or wind redistribution effects in the comparative PlanetScope image, and thus are less likely to deviate largely from the predicted values of the Random Forest approach (i.e., are unlikely to have high over-(under-)estimations typical for very thin snowpacks (avalanche cones)—Figure 9).

The derived random error estimate of the Pléiades snow depth map is found to be 0.36 m, with a small negative bias (−0.22 m) when comparing to a subdomain of the basin (Figure 7). The horizontal and vertical offsets applied in this study is found to be comparable with findings of snow depth derivation (Marti et al., 2016) and glacier mass change with co-registration (Berthier et al., 2014) using Pléiades 1A and 1B satellites. However, this level of error emphasizes Pléiades' inability to capture thin snow depths of the basin that are witnessed on northern slopes, low elevations or in the pro-glacial hummocky terrain at high elevations (Figure 10a). Additionally, this would suggest that this approach would be inappropriate for investigating snow depth distribution in the northern Chilean Andes where snow packs are typically shallow (e.g., Gascoin et al., 2013). Classifying shallow snow packs or snow absence using Pléiades DEM differencing therefore requires manual classification, machine learning approaches for image analysis (such the Gaussian mixture model applied here) or application of a normalized differential snow index to thermal band products to aid in the correction process.

Finally, we present here a high-resolution dataset for an entire catchment of ~102 km^2, though we are only able, given logistical constraints, to test the accuracy of Pléiades snow depths in detail for a lower segment of the total study site (Figures 6 and 7). While individual DEM values are within general agreement with high elevation LiDAR measurements for snow free areas, there are no temporally similar measurements that are well distributed within the catchment with which to validate the original or corrected snow depths presented. Nevertheless, this work highlights the sizeable deviations in information that may be derived from alternative models of snow depth estimations (section 3.7) even when the models are locally calibrated (Figure 11). Despite mean values of modeled snow depth remaining within the error ranges for Pléiades when corrected by other satellite information (Figure S3), we find that spatial variability of Pléiades snow depth is very different to the outputs of the model estimations (Figure 10).

5.3. Future Potential

To the knowledge of the authors, this is the first time that optical stereo triplets have been utilized to derive spatial snow depth information within the high elevation Andes range, a region of the world that has a relatively sparse observation network (Saavedra et al., 2018; Stehr & Aguayo, 2017). Pléiades snow depth maps, as presented here, offer a good alternative to many of the problems associated with obtaining snow depths using manual measurements or airborne or terrestrial LiDAR approaches (Marti et al., 2016). The dataset presented offers (i) a viable means of initial condition input for a hydrological modeling application, (ii) a test dataset with which to train statistical and dynamical models for future years (Grünewald et al., 2013), or (iii) a dataset for parameterizing local precipitation gradients or solid precipitation thresholds (Ayala et al., 2016). However, the Rio del Yeso catchment only represents ~2% of the total Maipo river catchment (4,837 km^2; Figure 1b) and therefore remains a small total area for training a statistical model for wider usage. Nevertheless, obtaining larger domains using Pléiades is feasible and would potentially offer more

cost effective means of deriving spatial snow depths than airborne LiDAR (e.g., Painter et al., 2016), though would ideally require carefully planned strategies to provide distributed ground based validation or an improved estimate of observation error (e.g., Bagnardi et al., 2016). However, although a systematic LiDAR scanning procedure at a range of elevations/orientations would be desirable for more rigorously modeling the errors of Pléiades, assuming a good distribution of sample snow-free pixels over static surfaces in the two DEMs, there can be sufficient information to calibrate the relative elevation differences. Future efforts within glacierized catchments also require a robust methodology for deriving winter snow accumulation over glaciers (Belart et al., 2017; Sold et al., 2013) though ideally with a $Snow_{OFF}$ DEM acquisition prior to the winter accumulation.

Marti et al. (2016) found ~22 and 14.5% of their 115 km^2 catchment with missing or negative data, respectively, identifying similar quantities of data which require correction to generate an end-product. Combined with the comparable bias offsets found between this study and the Pyrenean example, derivation of spatial snow depth using Pléiades stereo triplets appears to have consistent results, which is potentially valuable information for its future application. We recognize here, that replicability of our methodology requires data that may not be widely available (i.e., high-resolution ground-based LiDAR), though classification of surface type based upon the Pléiades orthoimages and open source approaches (Karasiak, 2019) are highly beneficial for correcting small/negative vertical differences evident from the Pléiades-derived DEMs.

6. Conclusions

In this study, we acquired two triplets of high-resolution optical images from the Pléiades satellites in order to generate spatial snow depth for a high mountain catchment of Central Chile with a horizontal resolution of 4 m. We recognize this as a recently developed methodology solely for snow depth derivation, though Pléiades-derived snow depths have yet to be tested for high mountain regions. Results of the Pléiades approach are negatively biased when compared against local observations of snow depth from a terrestrial LiDAR scan though distributed ground-based data are available for only a small subdomain of the study basin. Additionally, around one third of the original DEM differencing dataset (136 km^2) is subject to data gaps, negative values for shallow snow depths or noise on the steepest slopes (>40–50°). Accordingly, we adopt several steps in order to correct and filter the original snow depth map, using surface classification techniques and topographical parameters based upon the Pléiades elevation model (without snow). Comparing the corrected Pléiades snow depths to alternative topographical estimations and energy-balance model approaches, using locally calibrated data and PlanetScope satellite imagery, reveals between +54, and −28% difference in total snow volume for the catchment. The elevation-averaged snow depth relationship of the Pléiades data is similar to that suggested in the literature, with increase of snow depth until higher elevations, where removal of snow from wind and avalanching on steep slopes becomes dominant. Distributed snow depths relate well to elevation and aspect relative to north in a similar way to other studies in the northern hemisphere, though parameterizations based upon these studies fail to adequately prescribe the detailed variations that result from interactions of topographical features in our study catchment. Alternatively, physically based estimations of snow depth, using calibrated in-situ meteorological observations, are not able to sufficiently characterize snow variability at higher elevations and cannot resolve localized processes. Accordingly, the data offered by Pléiades represents an important contribution to understanding snow accumulation regimes at sparsely monitored or ungauged catchments in the central Andes, though its future usage ideally requires a careful validation procedure to identify biases and/or errors in the snow depth derivation.

Conflict of interest

We confirm that there are no conflicts of interest in the submission of this work.

Author contributions

All authors were involved in the planning of the research design. SG obtained and processed the raw Pléiades images in Ames Stereo Pipeline. PAM modified and executed the DBSM model. TES undertook field

data collection and wrote the manuscript. All authors contributed to the review and development of the manuscript.

Acknowledgments
The help of A. Caro, S. Quezada, B. Mir and L. Navarro for collecting field data is kindly acknowledged. This work recognizes funding from FONDECYT projects 3180145 (T. E. Shaw), 1171032 (J. McPhee) and 3170079 (P. A. Mendoza) as well as satellite imagery from the French space agency (CNES) and the PlanetLabs research and education initiative. This work has been supported by the CNES Tosca and the Programme National de Télédétection Spatiale (PNTS, http://www.insu.cnrs.fr/pnts), grant no. PNTS-2018-4. Data presented in this paper (cited as Shaw et al., 2019) are available at the following Zenodo online repository: https://zenodo.org/record/2551574#.XE9NLFxKiUk (10.5281/zenodo.2551574) with the exception of the raw Pléiades DEMs which are restricted by the regulations of the CNES agreement for grant PNTS-2018-4. We kindly recognize the valuable comments of scientific editor J. Lundquist and three anonymous reviewers that have helped to improve the quality of this work.

References

Ayala, A., McPhee, J., & Vargas, X. (2014). Altitudinal gradients, midwinter melt, and wind effects on snow accumulation in semiarid midlatitude Andes under la Niña conditions. *Water Resources Research*, *50*(4), 3589–3594. https://doi.org/10.1002/2013WR014960

Ayala, A., Pellicciotti, F., Macdonell, S., Mcphee, J., & Burlando, P. (2017). Patterns of glacier ablation across North-Central Chile: Identifying the limits of empirical melt models under sublimation-favorable conditions. *Water Resources Research*, *53*, 5601–5625. https://doi.org/10.1002/2016WR019804.Received

Ayala, A., Pellicciotti, F., Macdonell, S., Mcphee, J., Vivero, S., Campos, C., & Egli, P. (2016). Modelling the hydrological response of debris-free and debris-covered glaciers to present climatic conditions in the semiarid Andes of central Chile. *Hydrological Processes.*. https://doi.org/10.1002/hyp.10971

Ayala, A., Pellicciotti, F., Peleg, N., & Burlando, P. (2017). Melt and surface sublimation across a glacier in a dry environment: Distributed energy-balance modelling of Juncal Norte Glacier, Chile. *Journal of Glaciology*, *63*(241), 803–822. https://doi.org/10.1017/jog.2017.46

Bagnardi, M., González, P. J., & Hooper, A. (2016). High-resolution digital elevation model from tri-stereo Pleiades-1 satellite imagery for lava flow volume estimates at Fogo Volcano, 1–9. https://doi.org/10.1002/2016GL069457.Received

Belart, J. M. C., et al. (2017). Winter mass balance of Drangajökull ice cap (NW Iceland) derived from satellite sub-meter stereo images. *The Cryosphere*, *11*, 1501–1517.

Bernhardt, M., & Schulz, K. (2010). SnowSlide: A simple routine for calculating gravitational snow transport. *Geophysical Research Letters*, *37*(11). https://doi.org/10.1029/2010GL043086

Berthier, E., Arnaud, Y., Kumar, R., Ahmad, S., Wagnon, P., & Chevallier, P. (2007). Remote sensing estimates of glacier mass balances in the Himachal Pradesh (Western Himalaya, India). *Remote Sensing of Environment*, *108*(3), 327–338. https://doi.org/10.1016/j.rse.2006.11.017

Berthier, E., Vincent, C., Magnússon, E., Gunnlaugsson, P., Pitte, P., Le Meur, E., et al. (2014). Glacier topography and elevation changes derived from Pléiades sub-meter stereo images. *Cryosphere*, *8*(6), 2275–2291. https://doi.org/10.5194/tc-8-2275-2014

Best, M., Pryor, M., Clark, D., Rooney, G., Essery, R., Ménard, C., et al. (2011). The Joint UK Land Environment Simulator (JULES), model description—Part 1: Energy and water fluxes. *Geoscientific Model Development*, *4*, 677–699.

Breiman, L. (2001). Random Forests. *Machine Learning*, *45*(1), 5–32. https://doi.org/10.1017/CBO9781107415324.004

Brown, E., & Saldivia, J. E. (2000). Water management in Chile (in Spanish). Comité Asesor Técnico de América del Sur (SAMTAC), Asociación Mundial del Agua (GWP). [Available online at http://www.eclac.cl/DRNI/proyectos/samtac/InCh01100.pdf.].

Brown, R. D., & Mote, P. W. (2009). The response of Northern Hemisphere snow cover to a changing climate. *Journal of Climate*, *22*(8), 2124–2145. https://doi.org/10.1175/2008JCLI2665.1

Brun, F., Wagnon, P., Berthier, E., Shea, J. M., Immerzeel, W. W., Kraaijenbrink, P. D. A., & Arnaud, Y. (2018). Ice cliff contribution to the tongue-wide ablation of Changri Nup Glacier, Nepal, central Himalaya. *The Cryosphere*, *12*, 3439–3457.

Buhler, Y., Adams, M. S., Bosch, R., & Stoffel, A. (2016). Mapping snow depth in alpine terrain with unmanned aerial systems (UASs): Potential and limitations. *Cryosphere*, *10*(3), 1075–1088. https://doi.org/10.5194/tc-10-1075-2016

Burger, F., Ayala, A., Farias, D., Shaw, T. E., MacDonell, S., Brock, B. W., et al. (2018). Interannual variability in glacier contribution to runoff from a high-elevation Andean catchment: understanding the role of debris cover in glacier hydrology. *Hydrological Processes*.

Burger, F., Brock, B., & Montecinos, A. (2018). Seasonal and elevational contrasts in temperature trends in Central Chile between 1979 and 2015. *Global and Planetary Change*, *162*(April 2017), 136–147. https://doi.org/10.1016/j.gloplacha.2018.01.005

Cooley, S. W., Smith, L. C., Stepan, L., & Mascaro, J. (2017). Tracking Dynamic northern surface water changes with high-frequency planet CubeSat imagery. *Remote Sensing*, *9*, 1–21. https://doi.org/10.3390/rs9121306

Cornwell, E., Molotch, N. P., & McPhee, J. (2016). Spatio-temporal variability of snow water equivalent in the extra-tropical Andes Cordillera from distributed energy balance modeling and remotely sensed snow cover. *Hydrology and Earth System Sciences*, 411–430. https://doi.org/10.5194/hess-20-411-2016

Currier, W. R., Justin, P., Mazzotti, G., Jonas, T., Deems, J. S., Bormann, K. J., et al. (2019). Comparing aerial lidar observations with terrestrial LiDAR and snow-probe transects from NASA's 2017 SnowEx campaign water resources research. *Water Resources Research*, *55*, 6285–6294. https://doi.org/10.1029/2018WR024533

Deems, J. S., Painter, T. H., & Finnegan, D. C. (2013). Lidar measurement of snow depth: A review. *Journal of Glaciology*, *59*(215), 467–479. https://doi.org/10.3189/2013JoG12J154

Egli, L., Jonas, T., & Meister, R. (2009). Comparison of different automatic methods for estimating snow water equivalent. *Cold Regions Science and Technology*, *57*, 107–115. https://doi.org/doi.org/10.1016/j.coldregions.2009.02.008

Erxleben, J., Elder, K., & Davis, R. (2002). Comparison of spatial interpolation methods for estimating snow distribution in the Colorado Rocky Mountains. *Hydrological Processes*, *16*(18), 3627–3649. https://doi.org/10.1002/hyp.1239

Essery, R., Li, L., & Pomeroy, J. (1999). A distributed model of blowing snow over complex terrain. *Hydrological Processes*, *13*(14–15), 2423–2438. https://doi.org/10.1002/(SICI)1099-1085(199910)13:14/15<2423::AID-HYP853>3.0.CO;2-U

Falvey, M., & Garreaud, R. (2007). Wintertime precipitation episodes in central Chile: Associated meteorological conditions and orographic influences. *Journal of Hydrometeorology*, *8*(2), 171–193. https://doi.org/10.1175/JHM562.1

Fischer, M., Huss, M., Kummert, M., & Hoelzle, M. (2016). Application and validation of long-range terrestrial laser scanning to monitor the mass balance of very small glaciers in the Swiss Alps. *Cryosphere*, *10*(3), 1279–1295. https://doi.org/10.5194/tc-10-1279-2016

Freudiger, D., Kohn, I., Seibert, J., Stahl, K., & Weiler, M. (2017). Snow redistribution for the hydrological modeling of alpine catchments. *Wiley Interdisciplinary Reviews: Water*, e1232. https://doi.org/10.1002/wat2.1232

Garreaud, R., Alvarez-Garreton, C., Barichivich, J., Boisier, J. P., Christie, D., Galleguillos, M., et al. (2017). The 2010–2015 mega drought in central Chile: Impacts on regional hydroclimate and vegetation. *Hydrology and Earth System Sciences*, 1–37. https://doi.org/10.5194/hess-2017-191

Garreaud, R. D. (2009). The Andes climate and weather. *Advances in Geosciences*, *7*, 1–9.

Garreaud, R. D., Boisier, J. P., Rondanelli, R., Montecinos, A., & Veloso-aguila, H. H. S. D. (2019). The Central Chile Mega Drought (2010–2018): A climate dynamics perspective. *International Journal of Climatology*, (May), 1–19. https://doi.org/10.1002/joc.6219

Gascoin, S., Kinnard, C., Ponce, R., Macdonell, S., Lhermitte, S., & Rabatel, A. (2011). Glacier contribution to streamflow in two headwaters of the Huasco River, Dry Andes of Chile. *The Cryosphere*, *5*, 1099–1113. https://doi.org/10.5194/tc-5-1099-2011

Gascoin, S., Lhermitte, S., Kinnard, C., Bortels, K., & Liston, G. E. (2013). Wind effects on snow cover in Pascua-Lama, Dry Andes of Chile. *Advances in Water Resources*, *55*, 25–39. https://doi.org/10.1016/j.advwatres.2012.11.013

Grünewald, T., Buhler, Y., & Lehning, M. (2014). Elevation dependency of mountain snow depth. *The Cryosphere*, 2381–2394. https://doi.org/10.5194/tc-8-2381-2014

Grünewald, T., Schirmer, M., Mott, R., & Lehning, M. (2010). Spatial and temporal variability of snow depth and ablation rates in a small mountain catchment. *Cryosphere*, *4*(2), 215–225. https://doi.org/10.5194/tc-4-215-2010

Grünewald, T., Stotter, J., Pomeroy, J. W., Dadic, R., Moreno Baños, I., Marturiá, J., et al. (2013). Statistical modelling of the snow depth distribution in open alpine terrain. *Hydrology and Earth System Sciences*, *17*(8), 3005–3021. https://doi.org/10.5194/hess-17-3005-2013

Jagt, B., Lucieer, A., Wallace, L., Turner, D., & Durand, M. (2015). Snow depth retrieval with UAS using photogrammetric techniques. *Geosciences*, *5*(3), 264–285. https://doi.org/10.3390/geosciences5030264

Karasiak, N. (2019). Lennepkade/dzetsaka: Dzetsaka v3.4.4 (Version v3.4.4). Zenodo. http://doi.org/10.5281/zenodo.2647723

Lehning, M., Löwe, H., Ryser, M., & Raderschall, N. (2008). Inhomogeneous precipitation distribution and snow transport in steep terrain. *Water Resources Research*, *44*(7), 1–19. https://doi.org/10.1029/2007WR006545

Li, L., & Pomeroy, J. W. (1997). Probability of occurrence of blowing snow. *Journal of Geophysical Research*, *102*(D18), 21,955–21,964.

López-Moreno, J. I., & Nogués-Bravo, D. (2006). Interpolating local snow depth data: An evaluation of methods. *Hydrological Processes*, *20*(10), 2217–2232. https://doi.org/10.1002/hyp.6199

López-Moreno, J. I., Revuelto, J., Alonso-González, E., Sanmiguel-Vallelado, A., Fassnacht, S. R., Deems, J., & Morán-Tejeda, E. (2017). Using very long-range terrestrial laser scanner to analyze the temporal consistency of the snowpack distribution in a high mountain environment. *Journal of Mountain Science*, *14*(5), 823–842. https://doi.org/10.1007/s11629-016-4086-0

Marti, R., Gascoin, S., Berthier, E., De Pinel, M., Houet, T., & Laffly, D. (2016). Mapping snow depth in open alpine terrain from stereo satellite imagery. *The Cryosphere*, 1361–1380. https://doi.org/10.5194/tc-10-1361-2016

Mason, P. J., & Sykes, R. (1979). Flow over an isolated hill of moderate slope. *Quart. J. Roy. Meteorol. Soc*, *105*, 383–395.

McGrath, D., Sass, L., O'Neel, S., Arendt, A., Wolken, G., Gusmeroli, A., et al. (2015). End-of-winter snow depth variability on glaciers in Alaska. *Journal of Geophysical Research F: Earth Surface*, *120*(8), 1530–1550. https://doi.org/10.1002/2015JF003539

Mernild, S. H., Liston, G. E., Hiemstra, C. A., Malmros, J. K., Yde, J. C., & Mcphee, J. (2016). The Andes Cordillera. Part I: snow distribution, properties, and trends (1979 – 2014). *International Journal of Climatology*. https://doi.org/10.1002/joc.4804

Mernild, S. H., Liston, G. E., Hiemstra, C. A., Malmros, J. K., Yde, J. C., & McPhee, J. (2017). The Andes Cordillera. Part I: Snow distribution, properties, and trends (1979–2014). *International Journal Climatology*, *37*, 1680–1698. https://doi.org/10.1002/joc.4804

Meza, F. J., Wilks, D. S., Gurovich, L., & Bambach, N. (2012). Impacts of climate change on irrigated agriculture in the Maipo Basin, Chile: Reliability of water rights and changes in the demand for irrigation. *Journal of Water Resources Planning and Management*, *138*(5), 491–501. https://doi.org/10.1061/(ASCE)WR.1943-5452

Molotch, N. P., & Bales, R. C. (2005). Scaling snow observations from the point to the grid element: Implications for observation network design. *Water Resources Research*, *41*(11), 1–16. https://doi.org/10.1029/2005WR004229

Mott, R., Gromke, C., Grünewald, T., & Lehning, M. (2013). Relative importance of advective heat transport and boundary layer decoupling in the melt dynamics of a patchy snow cover. *Advances in Water Resources*, *55*, 88–97. https://doi.org/10.1016/j.advwatres.2012.03.001

Musselman, K. N., Pomeroy, J. W., Essery, R. L. H., & Leroux, N. (2015). Impact of windflow calculations on simulations of alpine snow accumulation, redistribution and ablation. *Hydrological Processes*, *29*(18), 3983–3999. https://doi.org/10.1002/hyp.10595

Nuth, C., & Kääb, A. (2011). Co-registration and bias corrections of satellite elevation data sets for quantifying glacier thickness change. *The Cryosphere*, *5*, 271–290. https://doi.org/10.5194/tc-5-271-2011

Painter, T. H., Berisford, D. F., Boardman, J. W., Bormann, K. J., & Deems, J. S. (2016). The airborne snow observatory: Fusion of scanning LiDAR, imaging spectrometer, and physically-based modeling for mapping snow water equivalent and snow albedo. Remote Sensing of Environment The Airborne Snow Observatory: Fusion of scanning lidar, imag. *Remote Sensing of Environment*, *184*(July), 139–152. https://doi.org/10.1016/j.rse.2016.06.018

Planet Team (2018). Planet Application Program Interface: In Space for Life on Earth; San Francisco, CA, USA; Available online: https://planet.com ().

Prokop, A. (2008). Assessing the applicability of terrestrial laser scanning for spatial snow depth measurements. *Cold Regions Science and Technology*, *54*(3), 155–163. https://doi.org/10.1016/j.coldregions.2008.07.002

Ragettli, S., Cortés, G., Mcphee, J., & Pellicciotti, F. (2014). An evaluation of approaches for modelling hydrological processes in high-elevation, glacierized Andean watersheds. *Hydrological Processes*, *28*(23), 5674–5695. https://doi.org/10.1002/hyp.10055

Ragettli, S., Pellicciotti, F., Immerzeel, W. W., Miles, E., Petersen, L., Heynen, M., et al. (2015). Unraveling the hydrology of a Himalayan watershed through integration of high resolution in situ data and remote sensing with an advanced simulation model. *Advances in Water Resources*, *78*, 94–111. https://doi.org/10.1016/j.advwatres.2015.01.013

Revuelto, J., Azorin-Molina, C., Alonso-González, E., Sanmiguel-Vallelado, A., Navarro-Serrano, F., Rico, I., & López-Moreno, J. I. (2017). Meteorological and snow distribution data in the Izas Experimental Catchment (Spanish Pyrenees) from 2011 to 2017. *Earth System Science Data*, *9*(2), 993.

Revuelto, J., López-Moreno, J. I., Azorin-Molina, C., & Vicente-Serrano, S. M. (2014). Topographic control of snowpack distribution in a small catchment in the central Spanish Pyrenees: Intra- and inter-annual persistence. *Cryosphere*, *8*(5), 1989–2006. https://doi.org/10.5194/tc-8-1989-2014

Rivera, A. (2012). Estimación de volúmenes de hielo mediante radio eco sondaje en Chile Central (in Spanish) - Centro de Estudios científicos S.I.T. 288, Santiago, November 2012.

Saavedra, F. A., Kampf, S. K., Fassnacht, S. R., & Sibold, J. S. (2018). Changes in Andes snow cover from MODIS data, 2000–2016. *The Cryosphere*, *12*, 1027–1046.

Scaff, L., Rutllant, J., & Rondanelli, R. (2018). Meteorological interpretation of orographic precipitation gradients along an Andes west slope basin at 30°S (Elqui Valley, Chile). *Journal of Hydrometeorology.*. https://doi.org/10.1175/JHM-D-16-0073.1

Schirmer, M., & Lehning, M. (2011). Persistence in intra-annual snow depth distribution: 2. Fractal analysis of snow depth development. *Water Resources Research*, *47*, W09517. https://doi.org/10.1029/2010WR009429

Shaw, T. E., Gascoin, S., Mendoza, P. A., Pellicciotti, F., & McPhee, J. (2019). Chilean Andes snow depth using Optical tri-stereoscopic remote sensing. *Water Resource Research*. https://doi.org/10.5281/zenodo.2551574

Shean, D. E., Alexandrov, O., Moratto, Z. M., Smith, B. E., Joughin, I. R., Porter, C., & Morin, P. (2016). An automated, open-source pipeline for mass production of digital elevation models (DEMs) from very-high-resolution commercial stereo satellite imagery. *ISPRS Journal of Photogrammetry and Remote Sensing*, *116*, 101–117. https://doi.org/10.1016/j.isprsjprs.2016.03.012

Sold, L., Huss, M., Hoelzle, M., Andereggen, H., Joerg, P. C., & Zemp, M. (2013). Methodological approaches to infer end-of-winter snow distribution on alpine glaciers. *Journal of Glaciology*, *59*(218), 1047–1059. https://doi.org/10.3189/2013JoG13J015

Stehr, A., & Aguayo, M. (2017). Snow cover dynamics in Andean watersheds of Chile (32. 0–39. 5 ° S) during the years 2000–2016. *Hydrology and Earth System Sciences*, *21*, 5111–5126.

Telling, J. W., Glennie, C., Fountain, A. G., & Finnegan, D. C. (2017). analyzing glacier surface motion using LiDAR data. *Remote Sensing*, *9*(283), 9–12. https://doi.org/10.3390/rs9030283

Trujillo, E., Ramírez, J. A., & Elder, K. J. (2007). Topographic, meteorologic, and canopy controls on the scaling characteristics of the spatial distribution of snow depth fields. *Water Resources Research*, *43*(7). https://doi.org/10.1029/2006WR005317

Vincent, C., Wagnon, P., Shea, J. M., Immerzeel, W. W., & Kraaijenbrink, P. (2016). Reduced melt on debris-covered glaciers: investigations from Changri Nup Glacier, Nepal. *The Cryosphere*, *10*, 1845–1858. https://doi.org/10.5194/tc-10-1845-2016

Winstral, A., Elder, K., & Davis, R. E. (2002). Spatial snow modeling of wind-redistributed snow using terrain-based parameters. *Journal of Hydrometeorology*, *3*(5), 524–538. https://doi.org/10.1175/1525-7541(2002)003<0524:SSMOWR>2.0.CO;2

Winstral, A., & Marks, D. (2014). Long-term snow distribution observations in a mountain catchment: Assessing variability, time stability, and the representativeness of an index site. *Water Resources Research*, *50*(1), 293–305. https://doi.org/10.1002/2012WR013038

Zheng, Z., Kirchner, P. B., & Bales, R. C. (2016). Topographic and vegetation effects on snow accumulation in the southern Sierra Nevada: A statistical summary from LiDAR data. *Cryosphere*, *10*(1), 257–269. https://doi.org/10.5194/tc-10-257-2016

Zhou, Y., Parsons, B., Elliott, J. R., Barisin, I., & Walker, R. T. (2015). Assessing the ability of Pleiades stereo imagery to determine height changes in earthquakes: A case study for the El Mayor-Cucapah epicentral area. *Journal of Geophysical Research: Solid Earth*, *120*, 8793–8808. https://doi.org/10.1002/2015JB012358

References From the Supporting Information

Cuffey, K. M. Paterson, W.B. (2010) *The physics of glaciers*. Fourth edition. Elsevier, Amsterdam: Elsevier. Amsterdam, etc., Academic Press. 704 pp. ISBN-10: 0-123694-61-2.

Farinotti, D., Huss, M., Fürst, J. J., Landmann, J., Machguth, H., Maussion, F., & Pandit, A. (2019). A consensus estimate for the ice thickness distribution of all glaciers on Earth. *Nature Geoscience*, *12*(March), 168–173. https://doi.org/10.1038/s41561-019-0300-3

Messerli, A., & Grinsted, A. (2015). Image GeoRectification And Feature Tracking toolbox: ImGRAFT. *Geosci. Instrum. Method. Data Syst.*, *4*, 23–34. https://doi.org/10.5194/gi-4-23-2015

Reid, T. D., & Brock, B. W. (2010). An energy-balance model for debris-covered glaciers including heat conduction through the debris layer. *Journal of Glaciology*, *56*(199), 903–916.